UC Merced

UC Merced Electronic Theses and Dissertations

Title

Colloidal Dynamics in an Anisotropic Environment

Permalink

https://escholarship.org/uc/item/2nc1g688

Author

Gireesan Sudha, Devika

Publication Date

2024

Copyright Information

Peer reviewed|Thesis/dissertation

UNIVERSITY OF CALIFORNIA, MERCED

Colloidal Dynamics in an Anisotropic Environment

A dissertation submitted in partial satisfaction of the
requirements for the degree

in

Physics

by

Devika Gireesan Sudha

Committee in charge:

    Professor Dustin Kleckner, Chair
    Professor Bin Liu
    Professor Daniel Beller
    Professor Linda S Hirst

2024

The dissertation of Devika Gireesan Sudha is approved, and it is acceptable in quality and form for publication on microfilm and electronically:

_____

(Professor Bin Liu)

_____

(Professor Daniel Beller)

_____

(Professor Linda S Hirst)

_____

(Professor Dustin Kleckner, Chair)

University of California, Merced

2024

DEDICATION

To the ones who taught me to bravely dream, who loved me enough
to let me go

EPIGRAPH

We are all born with a divine fire in us. Our efforts should be to give wings to this fire and fill the world with the glow of its goodness.

—DR. A.P.J. Abdul Kalam, Wings of Fire

TABLE OF CONTENTS

LIST OF FIGURES

x

ACKNOWLEDGEMENTS

I really enjoyed writing this thesis - the sum total of the work I have done in the last couple of years. I was 24 when I started the PhD program at UC Merced, now I'm 30. It was not just a major commitment in time but also time spent away from my family. I'm glad it translated into some meaningful.

In a long list of people to thank, I would like to begin with my thesis advisor, Prof Linda S Hirst. Thank you, Linda, for taking me in our lab, sending me to conferences, sending me to Kent State and Delaware to get trained and for all the support you have given me! Doing a PhD wasn't the hard part; finding and securing a job was. Being an international student on an expired visa, with home halfway across the globe , changed things. I'm very grateful to you for helping me navigate through things during the last couple of months. Thanks you so much!

To my collaborators at Kent State and Delaware, especially Dr Hend Baza and Dr David Rivas: I had a great time learning and discussing science with you. Thanks a ton! Dr Hend Baza, I have to say this - you are an aspirational woman in STEM! I hope to become the kind of researcher that you are.

Dr David Quint, my knowledge of the techniques and tricks of image analysis came from you. I'm so grateful for your help, time and guidance!

Dr Niranjan Sarpangala, Bhaiya your scientific temper and above all your kindness, are truly commendable. I hope to have you as a potential collaborator someday.

Dr Jeremias Gonzalez, I would have not survived this year if you weren't around. My favourite colleague, my go-to-person - you mean a lot to me! To have a mind like yours is a true blessing. If I had your mind, I would have been a MacArthur Fellow. I'm really gonna miss this - us discussing concepts, breaking down hard equations and for the most part, me yapping about something while you patiently listened. I hope we collaborate on a project in future.

Dr Ajay Khanna, you are one of the kindest and most caring people I have met. Thank you for everything that you have done for me!

Linda Jerome you remind me so much of my younger self. I'm so grateful for having you in my life. You and your family.

CURRICULUM VITAE

2013 - 2018	Integrated Bachelor of Science - Master of Science with a Major in Physics and Minor in Chemistry, Indian Institute of Science Education and Research (IISER), Thiruvananthapuram
2018 - present	PhD candidate in Physics, University of California, Merced

RESEARCH PROJECTS

Graduate Researcher in Hirst Lab, UC Merced   2019 - present

Colloidal aggregation in an anisotropic solvent.

Develop a novel self-assembling colloidal system to study particle aggregation in liquid crystal. Use fluorescent imaging and spatial correlation functions to investigate different stages of aggregation. Develop an aggregation model for anisotropic fluids to predict the structure and dynamics of large-scale aggregation and gelation.

Design a novel non-biological active nematic using Janus colloids in lyotropic chromonic liquid crystal.

Investigate the dynamics of individual active Janus colloids in nematic liquid crystal, propelled by a catalytic reaction and discover the key factors and parameters required to achieve collective motion.

Shapeshifting in liquid crystal

Investigate the formation of compact foam morphology in liquid crystal and understand the role of liquid-liquid phase separation in aggregate structure remodeling during nematic to isotropic phase transitions.

FELLOWSHIPS, AWARDS & HONORS

- Innovation in Science Pursuit for Inspired Research (INSPIRE) Scholar - Second Highest Undergrad Fellowship awarded in India in Science & Technology (2013-2018)

- AY 2018-2019 Physics Summer Fellowship

- AY 2019-2020 Physics Travel Award

- AY 2019-2020 Physics Summer Fellowship

- NSF Innovation Corps 2020, UC Merced for "One pot synthesis of nanoparticle-based micro-assemblies."

- AY 2020-2021 Physics Summer Fellowship

- AY 2020-2021 Physics Professional Development Fellowship

- Center for Cellular and Biomolecular Machines (CCBM) UC Merced Training Award 2022

- CCBM UC Merced Travel Award 2022

- AY 2021-2022 Travel and Development Fellowship

- Frontiers of Soft Matter and Macromolecular Networks Travel Award 2022

- Graduate Student Association UC Merced Travel Award 2022

- Physics Travel Award 2023

- Physics Summer Fellowship 2023

- MacKenzie Scott Graduate Student Supplemental Travel Award 2023

- Physics Travel Award 2024

- CCBM UC Merced Travel Award 2024

PUBLICATIONS

D.G. Sudha, J. Ochoa and L. Hirst, "Colloidal assembly and aggregation in an anisotropic solvent.", *Soft Matter*, 17, 2021.

D.G. Sudha, H. Baza, D. Rivas, S. Das, O. Lavrentovich, L.S. Hirst, "Behavior of chemically powered Janus colloids in lyotropic chromonic liquid crystal", *re-submitted to Physical Review E.*

D.G. Sudha, A. Wheeler, T. Atherton, L.S. Hirst, "From colloidal aggregates to foams – a novel method to make foams in nematic liquid crystal", *manuscript in preparation*

PRESENTATIONS

"Behavior of chemically powered active Janus colloids in a uniformly aligned nematic liquid crystal." D Gireesan Sudha, H Baza, D Rivas, S Das, O. Lavrentovich, L Hirst, APS March Meeting 2024, Minneapolis, MN, March 6, 2024.

"Motion of active Janus colloids in lyotropic chromonic liquid crystals." Liquid Crystals Gordon Research Seminar (GRS), Manchester, NH, June 25, 2023. (**Invited speaker**)

"Motion of active Janus colloids in lyotropic chromonic liquid crystals." D Gireesan Sudha, H Baza, D Rivas, S Das, O. Lavrentovich, L Hirst, APS March Meeting 2023, Las Vegas, NV, March 6, 2023.

"Self-assembled nanoparticle capsules and their aggregation in anisotropic liquid crystal solvent." D Gireesan Sudha, J Ochoa, L Hirst, APS March Meeting 2022, Chicago, IL, March 15, 2022.

"Self- assembled colloids and their aggregation in an anisotropic solvent." 95th ACS Colloid and Surface Science Symposium, (online), June 2021. (**Invited abstract**)

"Frank elasticity driven gelation and aging of self-assembled hollow colloids." D Gireesan Sudha, J Ochoa, L Hirst, ACS Spring 2021, (online), April 2021.

"Frank elasticity driven gelation and aging of self-assembled nanoparticle capsules." D Gireesan Sudha, J Ochoa, L Hirst, APS March Meeting 2021, (online), April 2021.

POSTERS

"Motion of active Janus colloids in lyotropic chromonic liquid crystals." D Gireesan Sudha, H Baza, D Rivas, S Das, O. Lavrentovich, L Hirst, Liquid Crystals Gordon Research Conference (GRC), Manchester, NH, June 2023.

"Self-assembled colloidal capsules and their aggregation in an anisotropic solvent." D Gireesan Sudha, J Ochoa, L Hirst, Frontiers of Soft Matter and Macromolecular Networks Conference, San Diego, CA, September 16, 2022.

"Self-assembled nanoparticle capsules and their aggregation in anisotropic liquid crystal solvent." D Gireesan Sudha, J Ochoa, L Hirst, 28th International Liquid Crystal Conference, Lisbon, Portugal, July 2022.

"Self-assembled colloids and their aggregation in an anisotropic solvent." D Gireesan Sudha, J Ochoa, L Hirst, Institute of Physics –Advanced School in Soft Condensed Matter 'Solutions in the Summer', (online), July 2021.

"One pot synthesis of quantum dots based hollow colloidal gel." CCBM Workshop on Emerging Themes in Cellular and Biomolecular Machines, Merced, CA, November 2019.

"Towards geometric control of quantum dot based hollow microstructures formed by two-stage nematic nucleation and phase separation." Summer School on Soft Solids & Complex Fluids, Amherst, MA, June 2019.

ABSTRACT OF THE DISSERTATION

Colloidal Dynamics in an Anisotropic Environment

by

Devika Gireesan Sudha

in Physics

University of California Merced, 2024

Professor Dustin Kleckner, Chair

Colloids are ubiquitous in nature and technology, playing vital roles in various fields, from pharmaceuticals to materials science. Liquid crystal colloids, formed by dispersing colloidal particles in a liquid crystal host, present a unique system where the interplay between the orientational order of the liquid crystal and the colloidal particles leads to complex, anisotropic interactions not seen in conventional colloidal systems. These interactions are characterized by the formation of topological defects and elastic deformations in the nematic order. This thesis aims to give insights into the fundamental physics at the intersection of liquid crystal and colloidal science, which can potentially lead to the development of advanced materials.

In the first part of the thesis, we investigate the aggregation behavior of colloidal particles in a nematic liquid crystal phase, which leads to the formation of hierarchical aggregate morphologies distinct from those in isotropic solvents. We developed a novel self-assembling colloidal system to study aggregation over large length scales involving thousands of colloidal particles. In this method hollow micron-scale colloids form *in situ* within the nematic phase and aggregate into fractal structures and colloidal gels. The morphology of these aggregates is determined by colloid concentration and temperature quench depth through the isotropic-to-nematic phase transition point. Using fluorescence microscopy, we measure the aggregate structure across various length scales, analyze ageing mechanisms, and

explore the driving forces behind aggregation. Our findings suggest that the aggregate dynamics are influenced by a combination of Frank elasticity relaxation, spontaneous defect line annihilation, and internal aggregate fracturing.

The second part of the thesis focuses on the interactions between active colloids and the anisotropic liquid crystal environment. For this work, we used platinum-coated Janus colloids, which exhibit self-propelled motion in aqueous solutions via the catalytic decomposition of hydrogen peroxide. When placed in a uniformly aligned nematic phase of lyotropic chromonic liquid crystal, disodium cromoglycate (DSCG), these active Janus colloids demonstrate motion that is strongly dictated by the anisotropy of the liquid crystal – they tend to move parallel to the nematic director. Motion analysis over a range of timescales reveals a cross-over from ballistic to anomalous diffusive behavior on timescales below the relaxation time for liquid crystal elastic distortions. Notably, we discover a size-dependent effect: smaller particles exhibit rolling motion during ballistic motion, whereas larger particles do not. This behavior highlights the complexity of phoretically-driven particle motion in the anisotropic fluid environment.

By investigating both the aggregation of passive colloidal particles and the motion of active Janus colloids, this thesis contributes to a deeper understanding of how anisotropic environments influence colloidal dynamics. These findings have the potential to help in the design of new materials and technologies that leverage the unique properties of liquid crystal colloids.

Chapter 1

Introduction

1.1 Motivation

The study of colloidal materials, where small droplets or particles of one material - typically ranging from 10nm to 10μm in size - are dispersed in a continuous phase of another material, has long been a central focus in material science research [1, 2]. When the continuous phase is a liquid crystal (LC), the resulting system is known as liquid crystal colloids [3, 4]. Liquid crystals are orientationally ordered fluid in which the molecules possess a degree of alignment or order along a preferred direction, while retaining the ability to flow. The directional order makes liquid crystals anisotropic.

The introduction of colloidal particles into a liquid crystal host has given rise to a new field at the intersection of LC and colloidal science, driven by the rich fundamental physics phenomena that arise from this unique combination. The interplay between the liquid crystal medium and the colloidal particles results in complex interactions and behaviors that are not observed in conventional colloidal systems. This combination of liquid crystal properties with colloidal particle dynamics offers possibilities for discovering new phenomena and developing advanced materials with technological applications.

One key difference between LC host and conventional isotropic host is that the molecular interactions at the interfaces of colloidal particles and the surrounding LC are highly anisotropic. When a spherical colloid with well-defined surface

anchoring is immersed in nematic liquid crystal, the alignment of the liquid crystal molecules near the surface of the colloid deviates from the bulk ordering of the liquid crystal. This deviation from the bulk alignment induces local disturbances in the nematic order, leading to the formation of topological defects. Topological defects are regions where the order cannot be defined, and at the core of the defect there is no specific molecular direction.

The disturbances caused by these defects spread over micrometer scales and can be considered as elastic deformations of the nematic liquid crystal. Since the elastic energy of these deformations depends on the separation between colloidal inclusions, they generate structural forces that are long-range and spatially highly anisotropic. These forces trigger the spontaneous assembly of neighboring colloids

The goal of this thesis is to understand the complexities and dynamics of colloid-nematic liquid crystal interactions. It covers the following two main topics

1.1.1 Aggregation behavior of colloidal particles within the nematic liquid crystal phase.

The motivation behind studying the aggregation mechanism, cluster growth and development in nematic liquid crystal host stems from the unique interactions that occur in anisotropic fluids, which are significantly different from those observed in isotropic solvents. Unlike in isotropic solvents, where colloidal aggregation follows well-understood patterns, the nematic phase introduces additional factors such as Frank elasticity and topological defect formation, leading to the formation of hierarchical aggregate morphologies distinct from those that tend to form in isotropic solvents [5].

Several groups have investigated these effects with relatively small numbers of colloids. For example, Mušević et al. [6] demonstrated the use of optical tweezers to position colloids into well-defined lattices stabilized by topological defects. Here, the equilibrium separation distance between two colloidal particles in the nematic phase is determined through a fine balance of elastic distortion energy minimization and topological defects, which prevent the particles from close approach. Several reports in this direction have shown that in small systems, colloidal particles can
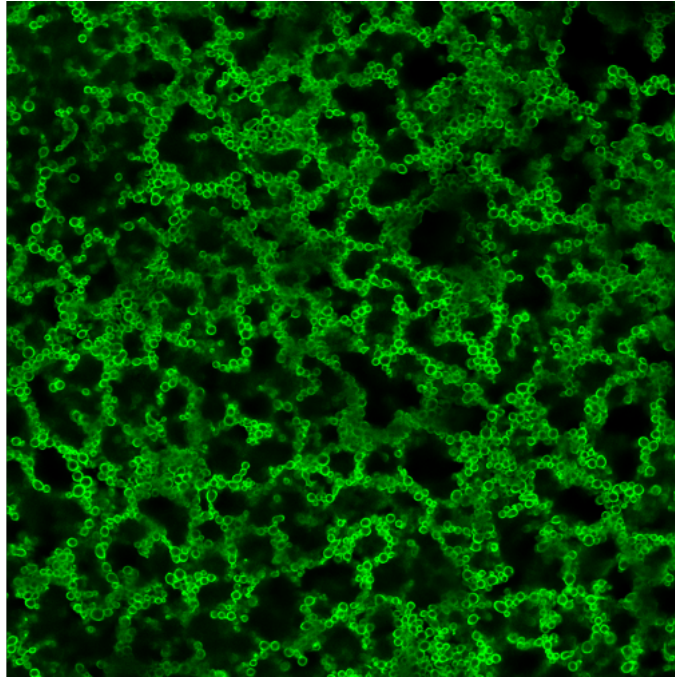
Figure 1.1: Hierarchical aggregate morphology formed within the nematic liquid crystal phase.

assemble into a variety of interesting morphologies, such as linear chains, [7, 8] anisotropic clusters, [9] particle stabilized defect gels [10] and two-dimensional nematic colloidal crystals [6]. These studies suggest that liquid crystal based colloid assembly may be useful for the creation of new optical materials. Most of the work on liquid crystal colloids has focused on either effective particle dispersion techniques [11–14] or topological defect configurations around small numbers of particles [15–18]. In contrast, conventional colloidal systems in isotropic solvents have an extensive literature on the structure and mechanisms of particle aggregation, with canonical examples being fractal growth in the diffusion limited and reaction limited regimes [19–21]. A significant limitation to performing analogous experiments in liquid crystal stems from the inherent difficulty in achieving a well dispersed initial state.

The question is: How to achieve an initial state for aggregation experiments? The goal is to develop a self-assembling colloidal system and investigate the mechanism for colloidal interaction and aggregate structure development. Understanding

these processes can not only deepen our knowledge of self-assembly mechanisms in anisotropic fluids but also potentially lead to the development of advanced materials with tailored properties.

Using a recently developed one-step process [22, 23], we were able to produce hollow, micron-scale colloids *in situ* in the nematic phase, which subsequently aggregate to form fractal structures and colloidal gels. The structure of these aggregates is determined by colloid concentration and the depth of temperature quenching through the isotropic-to-nematic phase transition point. This self-assembling colloidal system provides a unique method to study particle aggregation in liquid crystals over large length scales. I would like to emphasize that this colloid formation process is distinct from the methods described by Terentjev and colleagues [24–26], where dispersed 100nm to 150nm polymer spheres are cooled through the isotropic-to-nematic transition, forming open cellular structures as the particles become trapped by the growing nematic domains. In our method, the phase transition leads to the formation of separate hollow colloids.

1.1.2 Interactions of active colloids with the anisotropic liquid crystal environment

In nature, we have seen eye-catching displays of coordinated behavior among large group of moving animals. Flocking of sheep, starling murmuration, and schooling in fish - all these examples demonstrate how simple local interactions can lead to complex behaviors and patterns at a large scale [27, 28]. They come under collective behavior and emergent phenomena in the study of active matter.

Active matter refers to a system composed of self-propelling units, active particles, that convert ambient free energy into directed, systematic motion. The interaction of active particles among themselves and with the medium they live in, gives rise to highly correlated collective motion and mechanical stress, driving the system far from equilibrium. Unlike in passive systems, where equilibrium is eventually reached and dynamics cease, active matter remains in a state of continuous motion, breaking time reversal symmetry. This non-equilibrium nature allows for the emergence of complex patterns and structures with distinct orientational

Figure 1.2: Examples of collective behavior (from left to right) flocking of sheep, starling murmuration, and schooling in fish.

order, where particles align their directions of motion over large distances. Here, the emergence of orientational order is purely due to continuous activity.

The order parameter, as defined by the Vicsek model [28], is the average velocity vector of all the particles in the system, characterizing active polar systems. In such systems, particles exhibit polar alignment, and the model describes an abrupt change in order parameter - from randomly moving particles to particles aligning and moving in the same macroscopic direction - when the noise strength is decreased, or the concentration of particles is increased. Several recent studies have focused on the behavior of active particles dispersed in isotropic fluids, including self-assembly and their collective dynamics [29–31]. But what would happen if active particles were placed in a nematic liquid crystal? The simple answer is that the orientational order of the liquid crystal imposes a sense of direction. An exciting recent development in this field was the creation of "living liquid crystals". Such materials combine rod-shaped swimming bacteria with water-based liquid crystal, giving rise to an active nematic phase [32].

The goal is very ambitious: to develop non-biological active nematics using synthetic active colloids in lyotropic chromonic liquid crystals. Achieving this involves significant challenges, such as finding the right combination of particles and liquid crystals that can sustain consistent motion in the presence of fuel. The particles need to swim reliably over time, while the liquid crystal must provide an environment conducive to this activity, facilitating proper particle alignment. Moreover, coupling individual particle dynamics to global flows in the liquid crystal without causing aggregation adds further complexity. The project aims to discover the key

factors and parameters required for efficient particle propulsion, alignment with the liquid crystal, and avoidance of particle clustering. Given the complexity of the problem, we focus on understanding the dynamics of individual active particles within the nematic matrix. For this work, we selected chemically powered synthetic Janus colloids, driven by surface chemical reactions. These colloids typically propel themselves through self-diffusiophoresis or self-electrophoresis mechanisms [33,34].

This work complements the previously described modes of colloidal motion in a liquid crystal, reviewed recently [35]. In these systems, propulsion can be triggered by an externally applied electric field, which causes (i) a realignment of the director around a colloidal sphere and a backflow which displaces the particles [36–38]; (ii) Quincke rotation that converts into translation by interactions with the bounding walls [39, 40]; (iii) liquid crystal-enabled electro-osmosis in which a patterned director field is set into motion by an ac electric field [41]; (iv) liquid crystal -enabled electrophoresis, which requires fore-aft asymmetry of the director field around a colloid in order to separate the space charge in the applied electric field [42–50]. In the latter case, the fore-aft asymmetry can be created by homeotropic alignment of the director [42,43] but Hernàndez-Navarro et al. [47]and Devika et al. [48] demonstrated that a snowman-shaped colloidal particles with tangential anchoring create sufficient asymmetry to propel in an external electric field. For a Janus particle (see section 2.8 on Janus particle design), a possible slight fore-aft asymmetry of the director can also be caused by different anchoring conditions at the two hemispheres. Furthermore, Sahu et al. [49] discovered electrically powered propulsion of metal-dielectric Janus spheres in a thermotropic liquid crystal which sets quadrupolar rather than dipolar director deformations. In this case, the Janus asymmetry is sensed only by the electrostatics of the medium. From the point of view of symmetry of the director and the colloid, our work is similar to the work of Sahu et al. [49] as there is no clear fore-aft asymmetry of the director field. However, there are two key differences. First, the Janus sphere in our study is self-propelled, driven by internal mechanisms rather than by an external electric field. This self-propulsion introduces a dynamic component to the system that more closely mimics natural processes, potentially providing deeper insights into

active matter behavior.

Second, the medium in our study is a lyotropic liquid crystal rather than a thermotropic liquid crystal. This difference is critical because lyotropic liquid crystals are water-based, which makes them more biologically compatible. This compatibility opens possibilities for interfacing our system with biological materials, such as cell membranes or other biological tissues, where lyotropic liquid crystals can better mimic the native environment. Hence, our study not only deepens our understanding of active colloids in anisotropic media but can also be used for potential applications in bio-inspired materials and systems.

1.2   Outline of the thesis

In this thesis, we build on the topics discussed in previous sections to study the dynamics of passive and active colloids in nematic liquid crystal.

We begin Chapter 2 discussing the background theory, materials and experimental approach relevant to the projects discussed in this dissertation.

In Chapter 3, we study the aggregation dynamics and structural evolution of colloidal assemblies in nematic liquid crystal. We explain the experimental setup, including the self-assembling colloidal system used, and the analytical techniques employed, such as fluorescence microscopy and image analysis. Later, we discuss the key outcomes of the study focusing on the driving mechanisms behind these processes.

In Chapter 4, we investigate the motion of chemically powered Janus particles in a uniformly aligned nematic phase of lyotropic chromonic liquid crystal, disodium cromoglycate (DSCG). We discuss the experimental set-up, analytical techniques and outcomes of the study, focusing on how the liquid crystal's anisotropy directs self-propelled motion.

In Chapter 5, conclude with overall conclusions and future directions.

Chapter 2

Background Theory

In this chapter, I discuss the background theory required to understand the fundamental properties, behaviors and interactions of nematic liquid crystals. It starts with the concept of the nematic order parameter, a key descriptor of the orientational order within these liquid crystals. The chapter then discuss lyotropic chromonic liquid crystals, a specific class of mesophase that exhibit fascinating self-assembly behavior. Experimental tool like polarized optical microscopy to visualize the anisotropic properties, followed by the application of the Landau-de Gennes theory to describe the nematic phase and its transitions. As the chapter progresses, I discuss elastic distortions and topological defects that form in the nematic phase and the free energy cost associated with them. The interactions between colloidal particles and nematic liquid crystals are also discussed, highlighting how these interactions lead to unique self-assembly behaviors. Finally, I discuss about active colloids, which can add a dynamic element to the study of nematic systems.

2.1   Nematic order parameter

A nematic liquid crystal is a state of matter intermediate between an isotropic liquid and a crystalline solid. It can flow like a fluid, but its constituent molecules retain orientational order like solids. A nematic liquid crystalline phase is formed by the packing of elongated, rod-like molecules with their long axes parallel to each other. In this arrangement, the positions of the molecular centers of mass are

random, but they have long range order in orientational alignment of molecules. The direction of this average molecular ordering is called the director, denoted as $\hat{n}$. It is a unit vector that represents the main axis of nematic order. The degree of orientational order, which tells us how well the molecules are aligned with each other, is determined by the scalar order parameter S, written as [51–53]:

$$S = \left\langle \frac{3}{2}\cos^2\theta - \frac{1}{2} \right\rangle \tag{2.1}$$

Here, θ is the angle between the long axis of a selected molecule within the molecular ensemble and $\hat{n}$. The brackets $\langle\rangle$ denote the average of angular distribution over the ensemble of molecules. If $S = 0$ there is no alignment, and the system is in an isotropic phase. If $S = 1$, then it is fully aligned, the system is in a perfect nematic state. But the scale order parameter S alone can't fully describe the collective orientational ordering of molecules in space. For this, we need a tensor order parameter. Therefore, by combining S and $\hat{n}$ which describes the magnitude and direction of nematic order respectively, we can write a second rank tensor Q expressed as [54]:

$$Q_{\alpha\beta} = S \left[\frac{3}{2} n_\alpha n_\beta - \frac{1}{2}\delta_{\alpha\beta} \right] \tag{2.2}$$

This is only valid for the uniaxial nematic phase which has only one special axis $\hat{n}$, and n_α, n_β represent the components of $\hat{n}$ to give the full orientational description. The Q-tensor has two important properties, i) it is symmetric ($Q_{\alpha\beta} = Q_{\beta\alpha}$) ii) it is traceless ($Q_{\alpha\alpha} = 0$). $Q_{\alpha\beta}$ has three eigenvalues: S, $-S/2$ and $-S/2$. The eigenvector associated to S is $\hat{n}$. The eigenvectors corresponding to the other two eigenvalues are any direction perpendicular to $\hat{n}$. Because there are two degenerate eigenvalues of $-S/2$, all directions perpendicular to $\hat{n}$ are equivalent, i.e. there is rotational symmetry about $\hat{n}$.

2.2 Lyotropic chromonic liquid crystal

Lyotropic chromonic liquid crystal (LCLC) is a special class of lyotropic mesophase formed by the self-assembly of aromatic molecules in water. Common examples include disodium cromoglycate (DSCG), sunset yellow (SSY) [55, 56]. They are
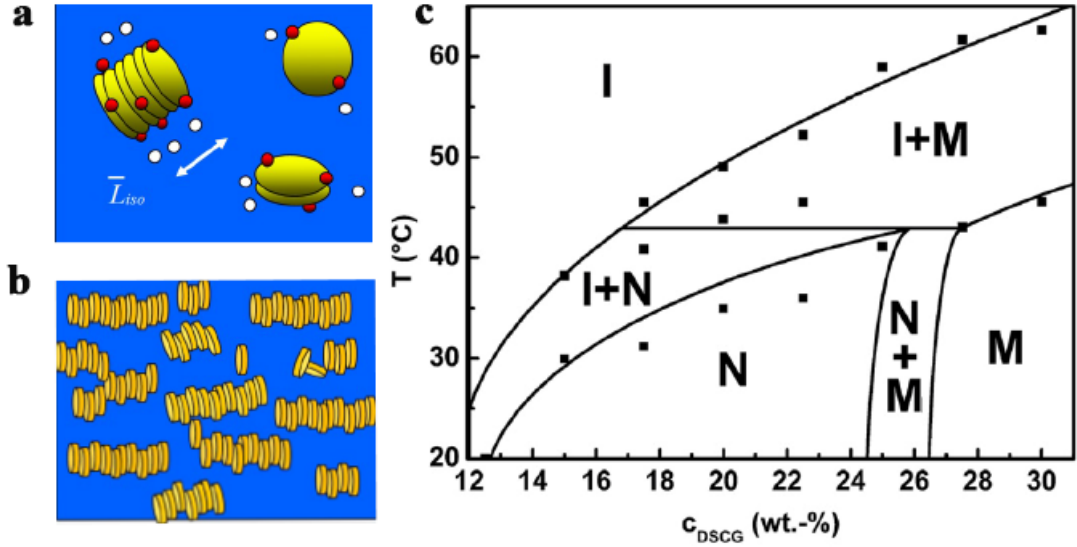
Figure 2.1: LCLC molecules form aggregate stacks and nematic phase. a) Face-face assembly of molecules to form an elongated cylindrical aggregate of average length $\overline{L}_{\text{iso}}$. b) Aggregate stacks forming a nematic phase. c) Phase diagram of DSCG as a function of temperature and concentration.

plank-like molecules with a polyaromatic central core and hydrophilic ionic groups at the peripheries. Once dissolved in water, these molecules aggregate face-to-face forming stacks with the ionic groups exposed at the aggregate-water interface. This aggregate stack forms the basic building block of LCLCs. Within the stack, the molecules interact through π-π attraction and the hydrophilic ionic groups at the interface make it water soluble. The energy required to break one aggregate into two called the scission energy E is the order of $10k_{BT}$. The LCLC aggregates are flexible making them different from conventional LCs made up of rigid rods. The flexibility is characterized by the persistence length λ_p, which is the length over which the direction of the tangent to the aggregates remains correlated. If the length of the aggregate is greater than λ_p, the aggregate is more flexible. The flexibility of the aggregates can also be influenced by the ion content which controls the Debye screening length λ_D. When the aggregate bend, the negative surface charges come closer and causes stronger electrostatic repulsion. A short λ_D, at high ionic content, effectively screen the negative charges relieving repulsion, and makes the aggregates more flexible. The average length of the aggregate in terms

of volume fraction ϕ of LCLC molecules, the temperature, the scission energy E and the diameter D of aggregate is [57]:

$$\overline{L}_{\text{iso}} = L_0 \phi^{5/6} \left(\frac{\lambda_P}{D}\right)^{1/3} \exp\left(\frac{E + k\phi}{2k_B T}\right) \tag{2.3}$$

where L_0 is the characteristic length of an LCLC molecule, k the constant taking into the excluded volume effects. Since L changes with temperature and concentration, we can control phase by varying these two parameters. Figure 2.1c shows the phase diagram for DSCG. At low temperature with increasing concentration, the length of the aggregate increases and eventually form a nematic (N) phase with aggregates aligning parallel to each other. There is a columnar (M) phase at high concentration wherein the stacks pack into a hexagonal array of extended columns.

2.3   Polarized optical microscopy

Liquid crystals are optically anisotropic. In a uniaxial liquid crystal, like DSCG, the optical properties vary along one specific axis called the director (or optic axis). The light passing parallel to the director experience a different speed and refractive index compared to the light passing perpendicular to the director. This anisotropy leads to birefringence, where light is split into ordinary and extraordinary rays, resulting in a phase difference between them. The phase difference depends on the difference in refractive indices, which varies with the wavelength of light due to dispersion. As the refractive index changes with wavelength, birefringence also varies, causing different wavelengths to undergo distinct phase shifts. This results in interference patterns that appear as a spectrum of colors under polarized light microscopy, allowing the visualization of the liquid crystal's optical properties.

In polarized optical microscopy, the birefringent material is placed between two crossed polarizers. In figure 2.2, the left polarizer is denoted as **P**, the right polarizer called the analyzer, is denoted as **A**. Non-polarized white light enters through **P** and is linearly polarized with an orientation in the direction indicated by the arrow. The polarized light then enters the birefringent material where it is refracted and divided into two mutually perpendicular components. The
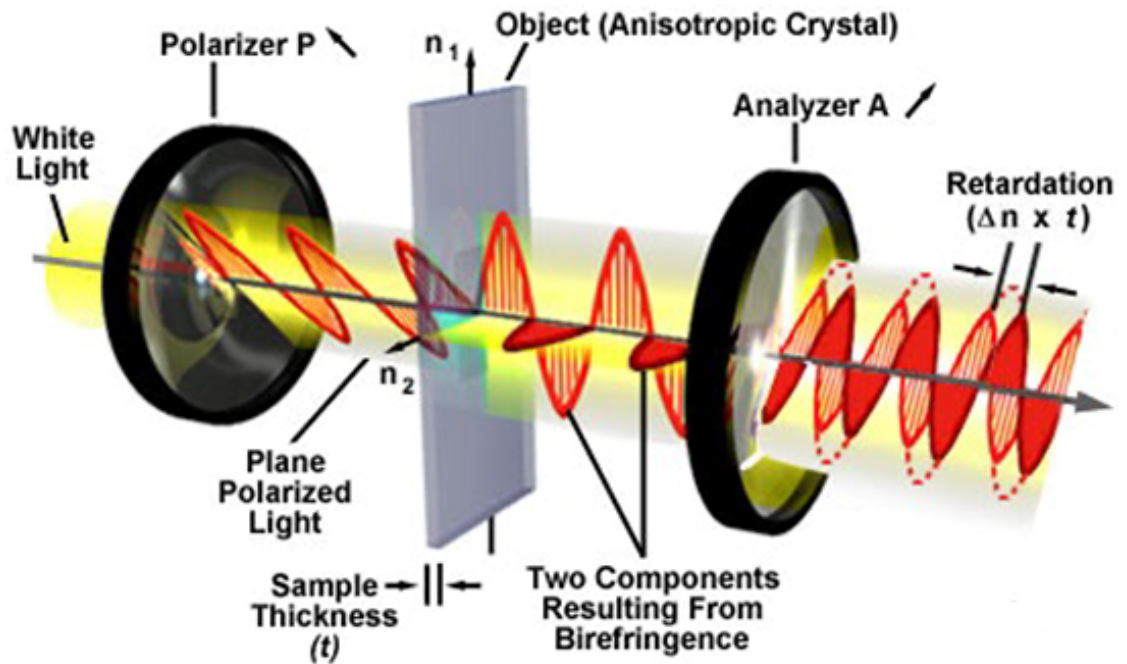
Figure 2.2: Birefringent material between crossed polarizers. Figure adapted from Olympus Life Science, "Birefringence", available at: https://www.olympus-lifescience.com/en/microscope-resource/primer/lightandcolor/birefringence/

difference in refractive indices associated with the ordinary and extraordinary rays or birefringence, is a measurable quantity expressed as an absolute value by the equation [58]:

$$B = |n_e - n_0| \tag{2.4}$$

As birefringence varies with wavelength, different wavelengths experience different phase shifts. When the light exits the birefringent material and passes through $\mathbf{A}$, these wavelengths interfere differently producing a spectrum of colors.

For a negative birefringent material like DSCG, $n_0 > n_e$. Their long axis is the "fast" axis which correspond to the extraordinary wave in this case. Light polarized in a plane parallel to the fast axis will pass through the crystal faster than light perpendicular to it as it experiences a lower refractive index. Consequently, the velocity of the ordinary ray is retarded compared to the faster ray, and the relative

retardation is given by:

$$\Gamma = t \cdot |n_e - n_0| \tag{2.5}$$

where t is the thickness. As the two rays exit the material, they interference constructive or destructive as they pass through the analyzer, creating a spectrum of colors as a result of wavelength dependent birefringence.

To determine the sign of birefringent material or the orientation of the nematic director, we can use accessory retardation plates. The retardation plate is also made of birefringent material and has its own perpendicular fast and slow axes. For the work carried out in Chapter 4 we inserted a full wave retardation plate, which introduce a phase difference of 2π between two orthogonal components of polarized light, at 45° with respect to the polarizer **P**. When the long (fast) axis of DSCG is aligned with the slow axis of the wave plate, we see a yellow-hued interference color. When the long (fast) axis is perpendicular with the slow axis, we see blue color.

2.4   Landau-de Gennes Theory

When $0 < S \leq 1$, the system is in nematic phase with molecules aligning preferentially in the direction of $\hat{n}$. When $S = 0$, the molecular orientational ordering is completely lost and the system transforms into an isotropic fluid phase. We can use Landau-de Gennes (LdG) theory [51–53, 59] to describe isotropic-nematic phase transition and determine the transition temperature and equilibrium order parameter. This theory is a macroscopic approach that involves expanding the free energy density as a function of the order parameter ($Q_{\alpha\beta}$) and finding the equilibrium configuration by minimizing the free energy. Since free energy is a scalar and $Q_{\alpha\beta}$ is a second rank tensor, to construct a scalar out of tensor the theory makes the following assumptions: i) free energy is a smooth function of the order parameter; we can write it as a power series in $Q_{\alpha\beta}$ and, ii) the order parameter is small; we can truncate the power series after a few terms. Thus, the free energy density is written as [51, 52, 59]:

$$f = f_0 + \frac{1}{2}A Q_{\alpha\beta}Q_{\alpha\beta} + \frac{1}{3}B Q_{\alpha\beta}Q_{\beta\gamma}Q_{\gamma\alpha} + \frac{1}{4}C \left(Q_{\alpha\beta}Q_{\alpha\beta}\right)^2 + \cdots \tag{2.6}$$

This can be further simplified by writing it in terms of S and $\hat{n}$. Using equation (2.2) we get,

$$f = f_0 + \frac{1}{2}aS^2 + \frac{1}{3}bS^3 + \frac{1}{4}cS^4 + \cdots \qquad (2.7)$$

where f_0 is the bulk free energy density associated with the isotropic phase ($S = 0$), $a = \frac{3}{2}A$, $b = \frac{3}{4}B$ and $c = \frac{1}{9}C$. Here the free energy is independent of $\hat{n}$, because no symmetry-breaking field is applied to the system, and the unknown coefficients a,b,c are considered to be smooth functions of temperature. When the parameters b and c were held fixed, with $b < 0$ and $c > 0$, and varying a linearly with temperature, the plots of LdG free energy density as a function of S appear as shown in Figure 2.3. At high temperature for large positive a, there's only one minimum at $S = 0$, corresponding to the isotropic phase (Figure 2.3a). On decreasing the temperature, a also decreases and there is a metastable nematic minimum at $S > 0$, along with the stable isotropic minimum at $S = 0$. As temperature continues to decrease, implicitly a is also decreasing, the nematic minimum becomes deeper. At a certain value of a, both minima becoming equally deep and a *first-order transition* from the isotropic phase to the nematic phase take place (Figure 2.3c). On lowering the temperature below the transition, there is a stable minimum at $S > 0$ in the nematic phase and a metastable minimum at $S = 0$ in the isotropic phase.

By minimizing the free energy and solving for $\frac{\partial f}{\partial S} = 0$, we get three real solutions: $S = 0$, $\quad S = \frac{-b \pm \sqrt{b^2 - 4ac}}{2c}$. Putting $S = \frac{-b - \sqrt{b^2 - 4ac}}{2c}$ into equation 2.7, we will find a at the isotropic-nematic transition point as $a_{IN} = \frac{2b^2}{9c}$ and the corresponding order parameter on the nematic side as $S = \frac{-2b}{3c}$. Using $a = a'(T - T_0)$ the isotropic-nematic transition temperature becomes $T_{IN} = T_0 + \frac{2b^2}{9a'c}$ [54].

2.5   Elastic distortions of the nematic order

In section 2.4, free energy depends on S but not on $\hat{n}$. The molecular interactions determine the magnitude of S but doesn't care about the orientation $\hat{n}$ of nematic order, unless $\hat{n}$ is spatially varying. If $\hat{n}$ is varying as a function of position, then the molecules are not as well aligned as they were if $\hat{n}$ was uniform.
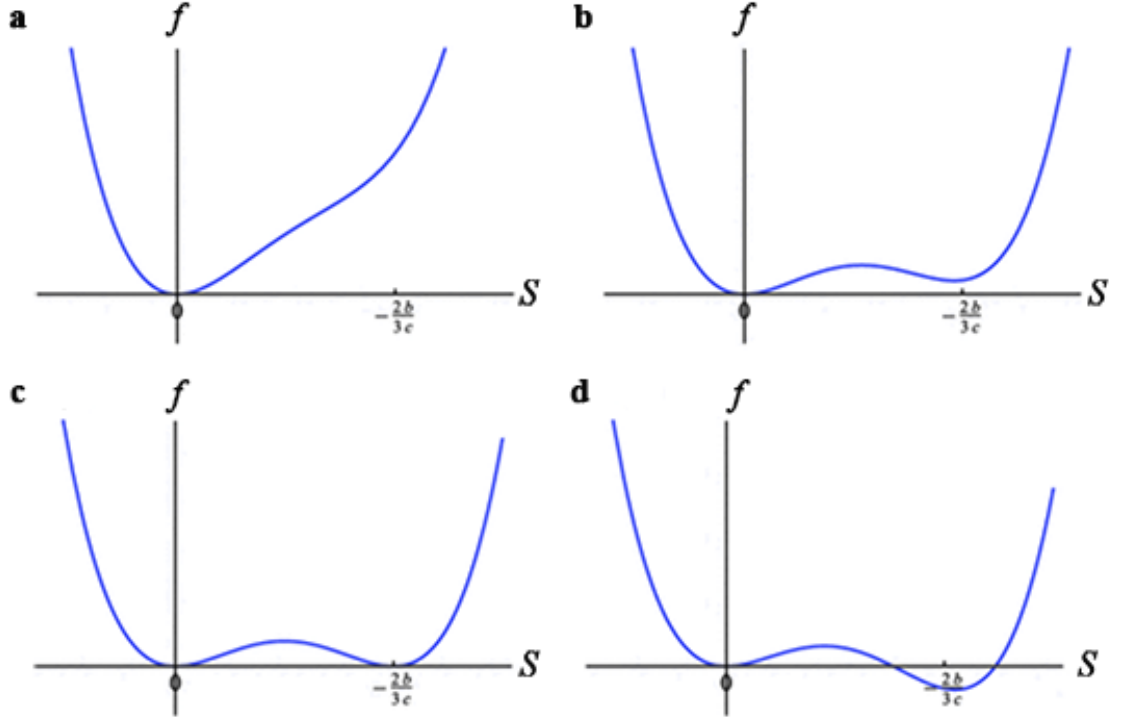
Figure 2.3: Plots of the Landau-de Gennes free energy density f as a function of the nematic order parameter S. a) Far above the isotropic-nematic transition. b) Slightly above the isotropic-nematic transition. c) At the the isotropic-nematic transition. d) Below the isotropic-nematic transition (reproduced from Selinger, 2016 with permission from Springer International Publishing) [54]

This adds an additional free energy term to equation (2.6) called the elastic free energy, or the Frank free energy [51, 61]. Starting with $\hat{n}(\mathbf{r})$ as the director field, that vary as a function of position, equation (2.2) can be re-written as:

$$Q_{\alpha\beta}(\mathbf{r}) = S\left[\frac{3}{2}n_\alpha(\mathbf{r})n_\beta(\mathbf{r}) - \frac{1}{2}\delta_{\alpha\beta}\right] \tag{2.8}$$

where $Q_{\alpha\beta}(\mathbf{r})$ is the tensor field specifying the nematic order for molecules near the position r. Including the gradients of $Q_{\alpha\beta}(\mathbf{r})$ and maintain appropriate symmetries, the LdG free energy density now becomes [54],

$$\begin{aligned} f = f_0 &+ \frac{1}{2}AQ_{\alpha\beta}Q_{\alpha\beta} + \frac{1}{3}BQ_{\alpha\beta}Q_{\beta\gamma}Q_{\gamma\alpha} \\ &+ \frac{1}{3}C_1\left(Q_{\alpha\beta}Q_{\alpha\beta}\right)^2 + \frac{1}{3}C_2Q_{\alpha\beta}Q_{\beta\gamma}Q_{\gamma\delta}Q_{\delta\alpha} \\ &+ \frac{1}{2}L\left(\partial_\gamma Q_{\alpha\beta}\right)\left(\partial_\gamma Q_{\alpha\beta}\right) + \cdots \end{aligned} \tag{2.9}$$

splay   *twist*   *bend*
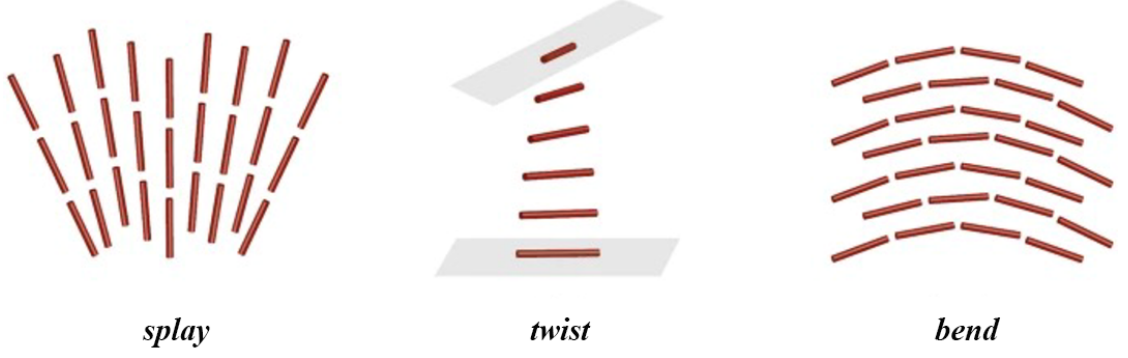
Figure 2.4: Three modes of elastic distortion; i) spay ii) twist and iii) bend. (reproduced from Van der Schoot, 2022, with permission from Springer International Publishing) [60]

The $\frac{1}{2}L\left(\partial_\gamma Q_{\alpha\beta}\right)\left(\partial_\gamma Q_{\alpha\beta}\right)$ term in equation (2.9) gives the free energy cost of varying any component of $Q_{\alpha\beta}$ in any direction r_γ. The coefficient L is the elastic constant, which depends on the material properties of the liquid crystal and quantifies the energy required to create distortions in molecular alignment. The elastic free energy term can be further simplified using the constraint that $\hat{n}(r)$ is a unit vector; $n_\alpha n_\alpha = 1$ The elastic free energy now becomes [54]:

$$F = \int d^3 r \left[\frac{1}{2}K(\partial_\gamma n_\alpha)(\partial_\gamma n_\alpha)\right] \tag{2.10}$$

where $K = \frac{9}{2}LS^2$. Equation (2.10) shows that variations of any director component n_α in any direction r_α cost free energy. Depending on the orientation of the local average $\hat{n}(r)$ and the varying component of $\hat{n}(r)$ with respect to the gradient direction, there are three modes of elastic distortion; i) spay ii) twist and iii) bend.

Equations 2.9 and 2.10 correspond to the "one elastic constant approximation", also known as "isotropic elasticity", where the three elastic constants associated with splay, twist and bend distortions are assumed to be equal and are denoted by a single elastic constant K. This is done for mathematical convenience and is often used in theoretical calculations, especially when the three elastic constants are relatively close in value. However, since the nematic liquid crystal is an anisotropic material, the actual free energy cost is different for different type of distortions. The free energy density contributions for the three modes of elastic distortions are the following, i) $f_{\text{splay}} = \frac{1}{2}K_1(\nabla \cdot \hat{n})^2$ ii) $f_{\text{twist}} = \frac{1}{2}K_2[\hat{n} \cdot (\nabla \times \hat{n})]^2$ iii) $f_{\text{bend}} =$

$\frac{1}{2}K_3[\hat{n} \times (\nabla \times \hat{n})]^2$, where K_1, K_2, and K_3 are the Frank elastic constants for splay, twist, and bend, respectively. Putting all these together, the more general form of the Frank free energy for elastic distortions in a nematic liquid crystal becomes,

$$F = \int d^3r \left[\frac{1}{2}K_1(\nabla \cdot \hat{n})^2 + \frac{1}{2}K_2[\hat{n} \cdot (\nabla \times \hat{n})]^2 + \frac{1}{2}K_3[\hat{n} \times (\nabla \times \hat{n})]^2 \right] \quad (2.11)$$

2.6   Topological defects in nematic

Topological defects are another type of director distortions that cannot just come and go continuously. They are regions of singularities of the director field, that appear as point defects called hedgehogs or defect lines called disclinations. Consider a 2D nematic phase, where the magnitude of nematic order S is fixed, and only the direction can vary. Let's say at any point, the direction of nematic order is given by the director $\hat{n}(r) = (\cos \phi(r), \sin \phi(r))$. Since in nematic phase both $\hat{n}$ and $-\hat{n}$ are the same, the direction of nematic order is represented using double-headed arrows. Suppose we have a director field configuration shown in Figure 2.5a, a local distortion in the center which cannot relax away. We can characterize the defect mathematically using *Burgers circuit*. A *Burgers circuit* is a closed loop drawn around the defect. After constructing a circuit (red circle) and monitoring the change in orientation of the director as we move in a counter-clockwise manner around the circuit, we will see ϕ increase from 0 to $\pi/2$, π, $3\pi/2$, and ends at 2π. Writing it as an integral we get $\oint d\phi = 2\pi$. Comparing this with Gauss's law in electrostatics, where the closed surface integral of the electric field over an arbitrarily shaped surface gives the total charge enclosed by that surface, we can use it to find the enclosed topological charge. So, the topological charge q enclosed inside the circuit,

$$\oint d\phi = 2\pi q_{\text{enclosed}} \quad (2.12)$$

From this we get a topological charge of $+1$ for Figure 2.5a. The topological charge in Figure 2.5 b,c are $+1/2$ and $-1/2$ respectively. As all defect configurations cause significant director distortions they accumulate lot of elastic energy. To determine the free energy cost for topological defects in 2D nematic phase, we can start by inserting $\hat{n}(r) = (\cos \phi(r), \sin \phi(r))$ into equation (2.10). Considering a single
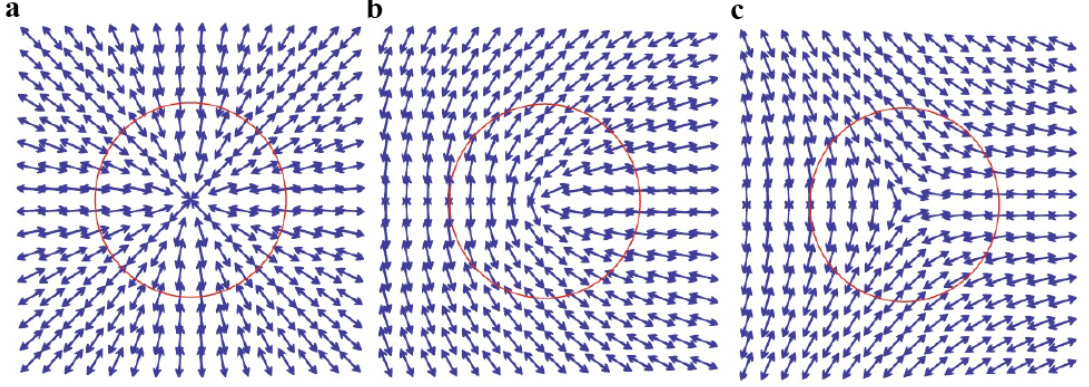
Figure 2.5: Topological defects in a 2D nematic phase with a topological charge of a) $+1$, b) $+1/2$ and $-1/2$. (reproduced from Selinger, 2016 with permission from Springer International Publishing) [54]

Frank constant, the free energy becomes,

$$F = \int d^2r \left[\frac{1}{2} K \left| \nabla \phi \right|^2 \right] \tag{2.13}$$

Although the uniform configuration (no topological defects) is the absolute minimum for free energy. The defect configuration $\phi(r)$ represents a local minimum, in the sense that no small changes in the director field can reduce the free energy further. The system is 'trapped' in this local minimum. However, small motions of the defect itself, through adjustments in the director field, can slightly lower the free energy. In this local minimum, the system satisfies the condition,

$$\frac{\delta F}{\delta \phi(r)} = -K \nabla^2 \phi = 0 \tag{2.14}$$

On solving this Laplacian and inserting it back into equation (2.13), we will get the free energy for a defect of topological charge q at the origin (Figure 2.5) as [54],

$$F = E_{\text{core}} + \pi K q^2 \log \left(\frac{R_{\text{max}}}{a} \right) \tag{2.15}$$

where E_{core} is the energy at the core of the defect, a the radius of the core which is typically the order of nanometers and R_{max} is the length scale of the sample that is distorted.
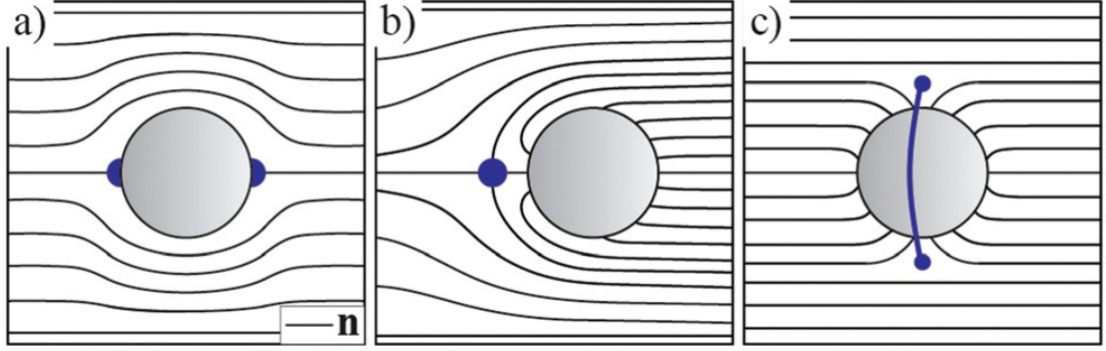
Figure 2.6: Nematic director profiles (black lines) near microspheres with a) a tangential anchoring showing surface defects dubbed as 'boojums'(quadrupolar symmetry), or homeotropic anchoring with b) a hedgehog defect (dipolar symmetry) or c) a Saturn-ring defect (quadrupolar symmetry). (reproduced from Kim et al., 2019, with permission from The Royal Society of Chemistry) [62]

2.7 Colloids in nematic liquid crystal

When a spherical colloid is introduced into a nematic liquid crystal, the liquid crystal molecules at the particle's surface align in a preferred direction due to the surface interaction. This alignment can be anchored in one of two ways: either normally (homeotropically) or tangentially (homogeneously) to the surface. This surface induced alignment creates a distortion in the surrounding nematic liquid crystal that extends over macroscopic distances, making the particle appear much larger than its actual size. This distortion is anisotropic due to the creation of topological defects, which are disruptions in the nematic order. These defects manifest as point defects (localized disruptions) or small loops of misaligned molecules near the particle's surface. These defects are fundamental and cannot be removed, following the law of conservation of topological charge, similar to the conservation of electric charge in electrostatics. The nature and extent of the distortion depend on the balance between the surface anchoring energy, which tries to align the liquid crystal molecules at the particle surface, and the bulk distortion energy, which resists this alignment. This balance is quantified by the deGennes–Kleman [3,51,63], $\xi_e = \frac{K}{W}$, where K is the average elastic constant measuring the free energy cost of splay, bend and twist elastic deformations and W is the anchoring strength. When the colloidal particle radius $R \gg \xi_e$ the surface anchoring dominates, strongly in-

fluencing the molecular orientation near the particle, resulting in a highly distorted director field. In contrast, when $R \ll \xi_e$ the elastic energy overcomes the surface anchoring, leading to a more uniform director field, though the surface molecules deviate from their preferred alignment.

When the colloidal surface favors homeotropic surface anchoring [3,6], there are two possible configurations of the distorted nematic around the colloidal particle, i) hyperbolic hedgehog defect, ii) Saturn ring. A hyperbolic hedgehog defect is a point defect with a topological charge of -1 and appear near the particle. The colloidal particle can be considered a source of a radial hedgehog defect, conceptually located at its center, carrying a topological charge of $+1$. This charge-compensating radial hedgehog together with the nearby hyperbolic hedgehog defect, forms a topological pair reminiscent of an electric dipole. This configuration is known as a topological dipole and is associated with a distorted director field exhibiting dipolar symmetry. The Saturn ring defect is a disclination loop which encircles the colloidal particle, resulting in a quadrupolar symmetry in the surrounding director field. When anchoring is tangential, the field distortion has quadrupolar symmetry with two surface boojums located at the particle-liquid crystal interface.

When several colloids are brought together, their regions of distortion overlap and interact, leading to structural forces between the particles. These forces which are elastic in origin, are long-range and highly anisotropic. As a result, the colloids self-assemble into two-dimensional (2D) structures, arranging themselves in a way that minimizes the system's total energy.

2.8   Active colloids

Active colloids are microscopic particles capable of autonomously moving through viscous fluids by harnessing and converting energy from their environment into directed motion. This category includes self-phoretic colloids, which generate their own gradients through internal mechanisms; field-driven colloids, which rely on external fields such as electric, magnetic, or acoustic fields for propulsion; and microorganisms like bacteria that use specialized appendages for movement. Their
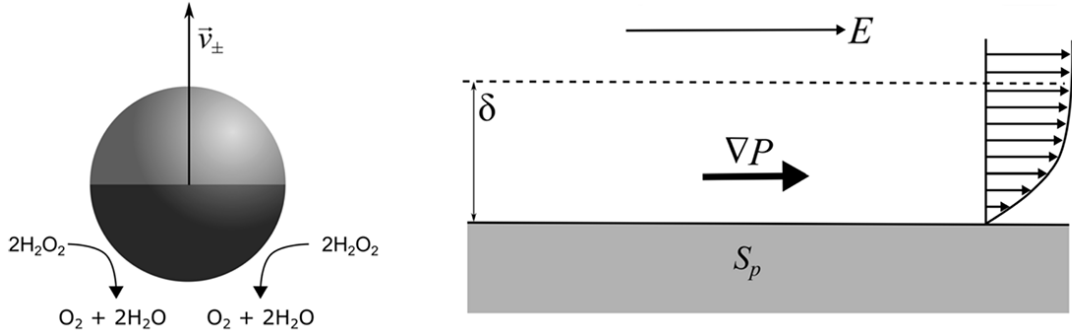
Figure 2.7: Schematic of self-generated phoresis. a) The asymmetric breakdown of hydrogen peroxide on the Pt side (dark patch) causes the Janus particle to move with a speed of $\pm v$, the direction of which depends on the local chemical environment. b) An self-generated electric field E interacts with the surface of the particle Sp creating a tangential pressure gradient ∇P which drives fluid flow. (reproduced from Longbottom and Bon, 2018, with permission from Springer Nature) [64]

continuous movement and energy consumption drive these colloids far from thermodynamic equilibrium, leading to complex dynamics and collective behaviors.

Active colloids often operate in viscous-dominated fluid environments where traditional methods of locomotion, such as reciprocal back-and-forth movement, fail to produce net displacement. This is due to the symmetry of forces at low Reynolds numbers. To overcome this, these colloids employ non-reciprocal mechanisms—motions or processes that do not reverse with time. By breaking time-reversal symmetry, they achieve sustained propulsion. In the case of Janus particles, this is achieved through their asymmetrical surface properties. This asymmetry breaks both spatial reflection and time-reversal symmetry, enabling continuous, directed movement despite the viscous drag of the fluid.

Named after the two-faced Roman god Janus, Janus particles are special type of colloidal particles with two distinct hemispheres. These hemispheres typically possess different physical or chemical properties, such as different materials or different functional groups. This duality allows Janus particles to exhibit a variety of asymmetric interactions with their environment, leading to behaviors that are not observed in isotropic colloids. For one of the thesis projects, we used Janus particles which were fabricated by capping one hemisphere of polystyrene (PS) spheres with a thin layer of metallic platinum (Pt). The PS side is fluorescent and

inert whereas the Pt side is active and non-fluorescent (see section 4.2.1). This contrasting Janus design allowed for the controlled study of particle dynamics - the active Pt side drives motion and the fluorescent PS side enables tracking and analysis through imaging techniques.

These engineered Janus particles exhibit self-propulsion when suspended in aqueous hydrogen peroxide (H_2O_2) solution. H_2O_2 is a reactive chemical that can decompose into water and oxygen (O_2) under certain conditions, $2H_2O_2 \rightarrow 2H_2O + O_2$. The Pt side interacts with H_2O_2 and catalyzes its decomposition creating a local concentration gradient of reaction products around the particle. This asymmetric chemical reaction generates a self-induced field E which interacts with the particle's surface Sp in the interfacial region δ, which is the thin layer of fluid immediately adjacent to the particle's surface. As a result of this interaction, a tangential pressure gradient ∇P is set along the surface of the particle, driving the movement of fluid around the particle. This flow generates an effective slip velocity along the particle's surface, which propel the particle forward. Typically, Janus particles propel with the PS side leading the way, by means of self-diffusiophoresis [33,65,66].

However, observations of ionic effects influencing propulsion direction, speed, and catalytic efficiency suggest electrophoretic contributions to the motion. Some researchers propose that ionic intermediates, such as superoxide (O_2^-) ions, play a crucial role in the propulsion mechanism by generating a localized electric field, which interacts with the particle surface. Others argue that neutral diffusiophoresis, driven by chemical gradients of non-ionic species like oxygen and water, might be the primary driving force. The precise mechanism remains a subject of debate, with ongoing studies exploring the relative contributions of surface roughness, Pt thickness, and asymmetry in catalytic activity. Further research, involving electrochemical measurements and controlled experiments, is also required to resolve this debate definitively [67,68].

Chapter 3

Colloidal aggregation in liquid crystal

In this chapter, I discuss the mechanism for colloidal aggregation and the subsequent structure development in liquid crystal solvent. Leveraging phase transition in liquid crystals, we developed a novel self-assembling colloidal system to study aggregation process over large length scales. Our observations using optical imaging and spatial correlation functions revealed that initial aggregation proceeds via mutual colloidal interactions is driven by Frank elasticity, followed by dramatic ageing effects characterized by defect annihilation and local compaction leading to the emergence of voids in the aggregate. The final aggregate structure ranges from dense gels, percolating networks to more tenuous fractals and isolated clusters. Our findings suggest that the continuously changing nematic director field around the growing cluster and presence of colloid-trapping line defects and loops makes this a complex many-body problem. Therefore, we need a new Elasticity Limited Cluster Aggregation (ELCA) model for anisotropic fluids to predict the structure and dynamics of large-scale aggregation and gelation.

3.1   Introduction

Colloidal aggregates are a feature of a wide range of natural and synthetic physical systems, where small, suspended particles tend to attract each other and

clump [69–72]. While the structure and formation dynamics of colloidal aggregates are well known in conventional, isotropic solvents, their properties in anisotropic solvents are less explored [73–76]. Generally, the stability of a colloidal system depends on the balance between particle–particle interaction forces, the gravitational force and thermal fluctuations. In dilute suspensions, a net attractive force between colloidal particles leads to the formation of fractal flocs which grow via cluster–cluster aggregation [19,73]. However, when colloidal particles are dispersed in an anisotropic fluid, such as the nematic liquid crystal phase, an effective force between particles arise due to Frank elasticity, an intrinsic property of the liquid crystal phase [54]. In the nematic phase, constituent molecules exhibit orientational order, defined by the director, $\hat{n}$. Over short length scales, these molecules tend to align and any deviation from this local alignment can be described by Frank elasticity theory in which deformations to uniform alignment are described by three elasticity parameters, splay, twist and bend (Chapter 2). When a spherical particle with well-defined surface anchoring is introduced into the phase, it frustrates the director locally causing elastic deformations around the particle, thereby increasing the free energy of the system. To minimize this energy cost, topological defects arise [3]. Consequently, when many particles are introduced into the nematic phase, they tend to group together, minimizing the free energy cost per particle.

While recent studies on the controlled assembly of colloidal particles in liquid crystals have attracted significant experimental and theoretical interest, research on aggregation mechanisms beyond the interactions of a small number of particles remains limited. This comes from the difficulties in creating an initial state for aggregation experiments. Using a recently discovered one-step process which produce hollow colloids that spontaneously self-assemble from dispersed nanoparticles as the system passes through the isotropic to nematic phase transition [22,23], we developed a novel method for the creation of well dispersed colloidal dispersions in liquid crystal *in situ*. The colloids produced in this method are micron-scale and form in the nematic phase with a random distribution. This method thus produces an excellent initial state for aggregation experiments, not easily acces-

sible by conventional colloid dispersion techniques such as sonication and is free from the effects of large-scale advective flows. Immediately after formation, the newly formed colloids respond to their liquid crystal environment and proceed to aggregate.

To form the colloids, individual surface-modified nanoparticles [77] were dispersed in the isotropic phase of the liquid crystal, then subjected to a rapid temperature quench through the isotropic to nematic phase transition (Figure 3.1) [22,23]. To perform the quench, the material is held slightly above the isotropic to nematic transition temperature (T_{NI}), and then transferred to a stage held at T, a temperature below the transition point. The quench depth, ΔT is equal to $T_{NI} - T$. After performing the temperature quench, colloids form within approximately one second. They are hollow, with walls composed of dense, randomly packed nanoparticles and range in size from 1–50μm. The size is controlled by quench depth and the concentration of nanoparticles [22]. Formation of these hollow colloids represents the starting point for this work, and it enabled us to investigate aggregation over large length scales using 1000s of colloidal particles.

Our experiments demonstrate how large-scale colloidal aggregation in liquid crystal produces significantly different morphologies to aggregates formed in ordinary isotropic solvents. The resulting structures are anisotropic on short length scales, with colloids organized into local chains. On medium to large length scales, they are fractal-like, increasing in overall density as colloid size decreases. Our analyses using pair correlation functions and particle velocimetry suggest that aggregate dynamics depend on a combination of Frank elasticity relaxation, spontaneous defect line annihilation and internal aggregate fracturing.

3.2   Experimental methods

3.2.1   One pot synthesis of colloidal aggregation in nematic liquid crystal

Following the method reported by Riahinasab et al. [22] a homogenous dispersion of ligand modified CdSe/ZnS core/shell quantum dots (QDs) was first prepared in the liquid crystal 5CB at 60°C, in the isotropic phase. A small drop
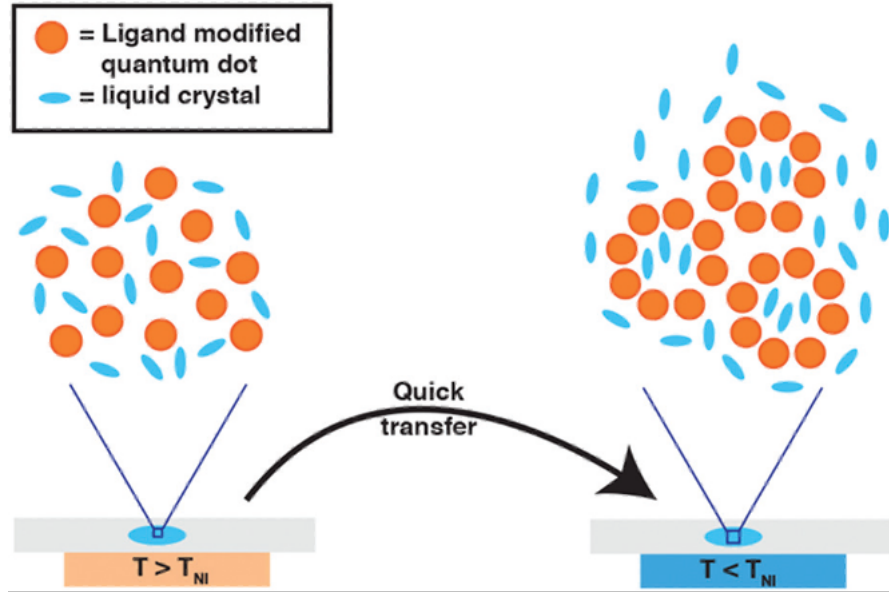
Figure 3.1: Schematic demonstrating the process of colloid formation. Well dispersed quantum dots in the isotropic phase (above T_{NI}) are rapidly transferred onto a lower temperature heat stage maintained at a temperature below T_{NI}.

of the above prepared solution was then pipetted onto a clean, warm glass slide with a 120μm thick spacer film. A coverslip was placed on top to slightly flatten the droplet. To ensure that the 5CB does not undergo the isotropic to nematic phase transition during cell construction, the microscope slides were assembled inside an oven held at 60°C. Then, using a hot copper block, the assembled glass slides with liquid crystal droplet were placed on a heat stage maintained at 50°C. From the 50°C heat stage, the glass slide containing the droplet is quickly transferred to an adjacent temperature stage maintained at a temperature below the isotropic–nematic transition temperature (T_{NI}). This transfer made the liquid

crystal droplet to undergo an isotropic to nematic phase transition in a rapid quench. Depending on the temperature difference (quench depth) between heat stages, the dispersed quantum dots organized into micron-sized assemblies with distinct morphologies [22]. We used quench conditions that favor the formation of small, single compartment hollow colloids in most experiments. The so formed hollow colloids attract each other and clump to form aggregates. The QDs forming the colloid walls were previously shown to have an average interparticle spacing of 12.94nm [23] and are high temperature tolerant due to the presence of ligand [77].

3.2.2   Fluorescence microscopy

Images were taken with a Leica DM2500P upright reflection microscope using a 10x objective. Because the aggregates are composed of colloids formed from quantum dots, (emission wavelength 620nm), we selected a 450–490nm band-pass filter for excitation. Emission was detected using a 510nm dichroic mirror and a 515nm long pass filter. Videos were recorded using an QImaging Retiga Exi camera at 1s time intervals with a 33.33ms exposure time for the first 2min after transfer to the microscope mounted heating stage. Later images were recorded at 10s intervals for 30min. Additional characterization of the aggregates was performed using images taken with a Zeiss LSM 880 confocal microscope, with Airyscan detector. To overcome the quasi-two-dimensional (2D) effect while taking a 2D image from a three-dimensional sample, the z-resolution was kept smaller than the average colloid size by making appropriate choice of objective lens and numerical aperture (objective plan-apochromat 63x/1.4 oil DIC M27, objective w plan-apochromat 20x/1.0 DIC M27 75mm, objective plan-apochromat 10x/0.45). The resulting images were remarkably clear on the smallest length scales of our experiment, with individual colloids and their hollow interiors resolved well. Combining this resolution with tile-scanning allowed us to probe structure over a particularly wide range of length-scales (from $0.8\mu m$ to $1000\mu m$).

3.2.3   Image processing

Prior to analysis, confocal tile scan images were post processed to minimize noise and reduce motion blur. The fluorescence images, consisting of discrete hollow colloids on a dark background, required precise localization of colloids within the aggregate. However, shading effects observed during fluorescence imaging caused intensity variations that did not directly reflect mass density, as lower intensity did not necessarily mean less mass. To address these issues and accurately show both the position of the colloids and the mass distribution, we performed the following multi-step protocol in ImageJ. (1) Background subtraction - a local background value for every pixel was determined using the rolling ball algorithm. The rolling ball radius was set to be equal to the average size of the colloids, in pixels. These background intensity values were then subtracted from the original image to remove any large background intensity variations in the image. (2) To further reduce noise and to smooth the image, a median filter was used. This filter replaces each pixel value with the median of its neighboring pixel values, while preserving the edges. The filter radius was set equal to the average thickness of the colloid walls in pixels. (3) A second background subtraction was also performed to further minimize spatial intensity variations. This time the rolling ball radius was kept much smaller. (4) Binary image masking - to clearly separate colloid pixels from background pixels, we set the value of a background pixel to 0 and the object pixel to 1. To create the binary mask, we first converted the processed image to 8-bits, then adjusted the binary threshold to an appropriate value. Everything below a threshold value was converted to 0 (background). After binarizing the image, we used the 'remove outliers' tool, skeletonized the binary image and then dilated it twice afterwards. Pixel values were divided by 255 to create the binary mask. (5) The raw data was then multiplied by the binary mask to obtain the final image, which was used for analysis.

3.3 Analysis techniques

3.3.1 Pair auto-correlation function

The confocal tile scan images depict hollow colloids, densely packed into a gel-like aggregate, it was fairly difficult to perform image segmentation to determine exact colloid positions. Therefore, we calculated the pair correlation function of the entire aggregate using a Fast Fourier Transform method described by Veatch et al. [78] to quantify colloidal organization. The pair auto-correlation function $g(\vec{r})$ gives the probability of finding a particle at a distance r from a given particle and is calculated using the expression,

$$g(\vec{r}) = \frac{\text{FFT}^{-1}\left(|\text{FFT}(I)|^2\right)}{\rho^2 N(\vec{r})} \tag{3.1}$$

here FFT^{-1} is the inverse Fast Fourier Transform, I is a matrix representing the pixel intensity on the post processed binary confocal tile scan image, ρ the average particle density and $N(\vec{r})$ is a normalization factor accounting for the finite size of the image, given as the autocorrelation of a window function W that has a value of 1 inside the measured area [78]

$$N(\vec{r}) = \text{FFT}^{-1}\left(|\text{FFT}(W)|^2\right) \tag{3.2}$$

The normalization factor $N(\vec{r})$ takes into account the fact that there are fewer possible pairs separated by large distances for a finite image size. Both I and W are padded by equal numbers of zeros in both directions to a distance larger than the image size, to avoid artifacts coming from the periodic nature of the FFT function. For a random distribution, the pair correlation function is equal to 1. In a random distribution of small colloidal clusters, $g(\vec{r}) > 1$ at length-scales below the average cluster radius and tends towards 1 at longer length-scales [79, 80]. In our system, this measure can be used to characterize two different features of the aggregates. First, the hollow colloids that make up the entire structure have a discrete size and pack closely with their neighbors. Secondly, the colloids are organized on a larger scale into more tenuous or gel-like structures. The pair correlation function can be used to quantify both of these structural features and in the case of fractal

aggregation, is expected to follow the power law, $g(\vec{r}) \propto r^{D_f - d}$, where D_f is the fractal dimension of a fractal aggregate and d is the spatial dimension [81].

3.3.2 Velocity autocorrelation function

To investigate how the velocity of colloids at different spatial locations are related during aggregate formation and ageing, we calculated the spatial auto-correlation function of the velocity field. To obtain the velocities we used Particle Image Velocimetry (PIVLab) software [82]. This software calculates the positional cross-correlation between consecutive movie frames separated by a small-time interval, dt. Prior to analysis the time stacks of images were converted to 8-bit images, then noise reduction using background subtraction and the median filter in ImageJ was performed. Time stacks were then imported to PIVlab and the image sequencing style set to time resolved A–B, B–C, C–D. . . mode, where A represents the image taken at first instance, B the second instance, etc. Images were grouped into frames, where each frame is a pair of images taken dt (in our case 1s or 10s) apart. Using the 'FFT window deformation' correlation algorithm in PIVlab, the displacement in each frame was calculated. We obtained data for u and v, the position-dependent velocities in the horizontal and vertical directions respectively and calculated the spatial velocity autocorrelation function for each movie frame.

The spatial velocity autocorrelation function (VACF) gives insights into the dynamics of colloidal motion during aggregate formation and ageing, and is complementary to the mass correlation function $g(\vec{r})$ in Figure 3.8 [83]. When expressed as a function of distance it is written as,

$$\psi(r) = \frac{\langle v(\vec{R}) \cdot v(\vec{R} - \vec{r}) \rangle}{\langle v_{\mathrm{norm}}^2 \rangle} \tag{3.3}$$

where $v(\vec{R})$ and $v(\vec{R} - \vec{r})$ are the velocities of particles at two different locations. $\langle \ldots \rangle$ represents the average over all $\vec{R}$. $v(\vec{R})$ has components $u(\vec{R})$, $v(\vec{R})$, the horizontal and vertical components respectively, which we obtain from PIVlab for each movie frame.

This calculation yields a value of $\psi(r) = 1$ for perfectly correlated velocities, $\psi(r) = 0$ for no correlation and -1 for anticorrelation, i.e. the two points have velocities in opposing directions. We used movies with frames separated by a time interval $dt = 10$ s and averaged the spatial VACF over the number of frames used in the selected time intervals. As the colloidal capsules move at a faster rate at early times, VACF analysis for the inset was performed on frames separated by a time interval $dt = 1$s and averaged over 21 frames. Figure 3.9 shows the time dependence of VACF over the initial and longer time intervals.

3.4 Results

3.4.1 The process of aggregate formation

Under fluorescence microscopy, the liquid crystal remains invisible while the quantum dots which make up the hollow colloid fluoresce. We performed several aggregation experiments at different quench depths, recording movies of the aggregation process using fluorescence microscopy. Figure 3.2 (a–f) shows a typical image time sequence for an aggregate formed after a ($\Delta T = 20°$C) quench. Figure 3.2a (t = 0 s) represents the start of the experiment immediately after the quench. The generally bright, uniform fluorescent background in Figure 3.2a is indicative of uniformly distributed, individual quantum dots that have not yet formed into colloids. With a diameter of approximately 10nm, we do not expect to optically image the nanoparticles. Some subtle inhomogeneity is observable in the image, indicating that the colloids have begun to form slightly out of the focal plane, close to the lower glass surface. At t = 10 s (Figure 3.2b) the colloids are fully formed (the formation process takes approximately 1s) and suspended in the nematic phase with a random distribution. The following images (Figure 3.2 (c–f)) illustrate the different stages of a typical aggregation sequence.

Once formed the dispersed colloids move towards each other through the nematic liquid as if mutually attracted. On close approach they stick together to form an aggregate. The final aggregates typically consist of connected linear chains of colloids, that tend to form a web-like arrangement over short length-scales. On
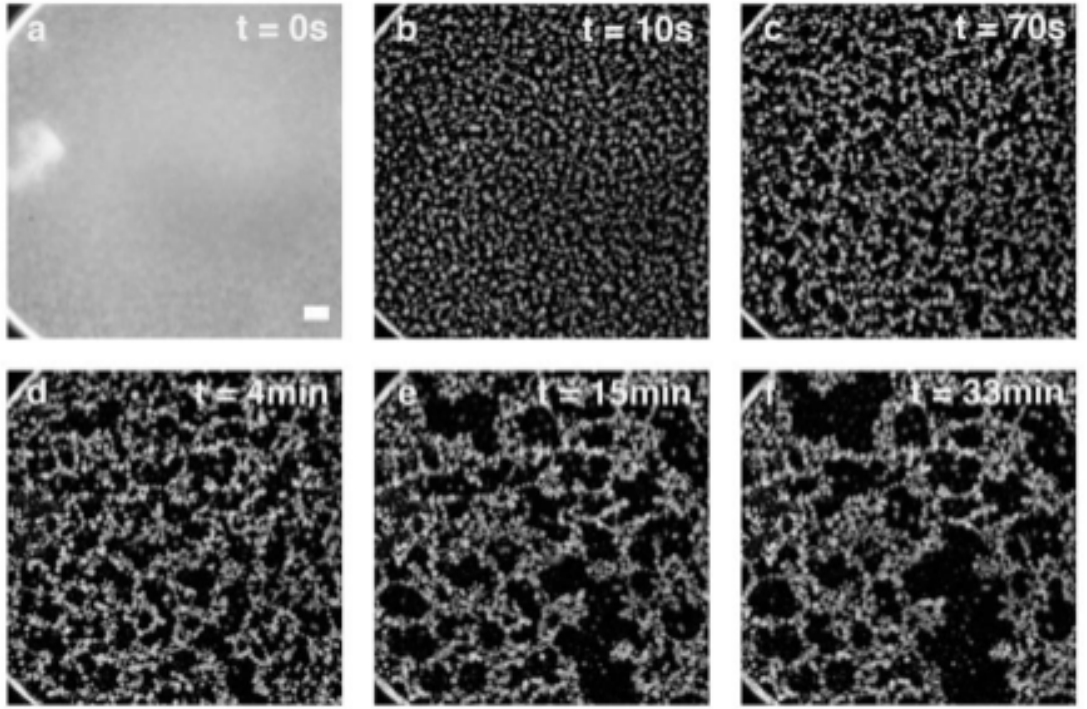
Figure 3.2: Fluorescence microscope images of colloids during aggregation and aging process. Fluorescence microscopy images of aggregate formation captured over 33min (a–f) using a quench depth $\Delta T = 20°$C with 0.30 wt% of ligand modified quantum dots (QDs) in the nematic phase of 5CB (scale bar $= 100\mu$m).

length-scales $> 200\mu$m they appear isotropic and include voids of various sizes with a fractal-like appearance. To complement the standard fluorescence microscopy, we performed more detailed imaging using a tile-scanning confocal fluorescence microscope (Figure 3.3 (a-c)). These images highlighted the remarkable hierarchical nature of the aggregates, from individual colloids to large length scales. Starting with 6nm quantum dots that self-assembled into hollow colloids around 5μm in diameter, to these colloids further grouping together into aggregate morphologies spanning several millimeters. The one-pot method enabled us to achieve significant jumps in length-scales.

The nature of attractive inter-colloid potential in this system is fundamentally different to that between colloids dispersed in an ordinary solvent such as water, where van der Waals forces and electrostatics typically dominate. In an anisotropic fluid, such as the nematic phase, short-range interactions between colloids derive
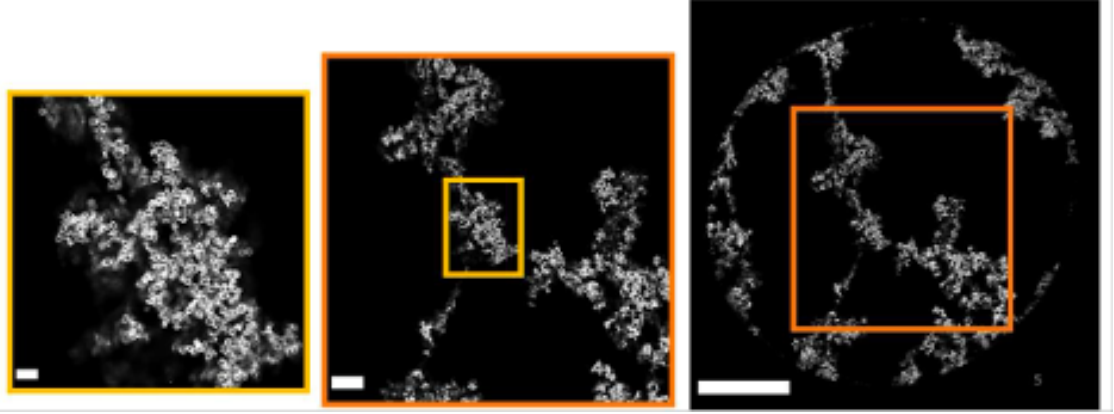
Figure 3.3: (a-c) Fluorescence confocal tile scan images of an aggregate formed with a quench depth $\Delta T = 30°$C, and concentration of 0.15wt% of ligand modified QDs highlighting the hierarchical nature of the aggregate. Scale bar = a-20μm, b-100μm and c-500μm

primarily from local deformations of the liquid crystal host phase. This process has been previously explored for pairs and small numbers of colloids by several groups [5,6,84] revealing the role of Frank elasticity and topological defects around neighboring colloids in attracting and binding them together. Structures can be predicted and manipulated externally for small systems (e.g., tens of colloids). In large systems, however (i.e., hundreds to thousands of colloids) aggregation have not been broadly investigated and the resulting structures have not been reported. The mechanisms underlying aggregation and ageing in anisotropic fluids are not well understood. Careful microscopic observation of the aggregation process depicted in Figure 3.2 (a–f) revealed several interesting phenomena that provided insights into the physical mechanisms driving larger-scale colloidal aggregation in liquid crystal (discussed in the up-coming next sections).

3.4.2 Colloidal chains and defect lines

The ligands on our colloids impart tangential anchoring conditions [29] that produce local topological defects around each spherical particle in the nematic phase. For small numbers this induces their organization into kinked chains. Although like previous observations of chaining for colloidal aggregation in an isotropic sol-
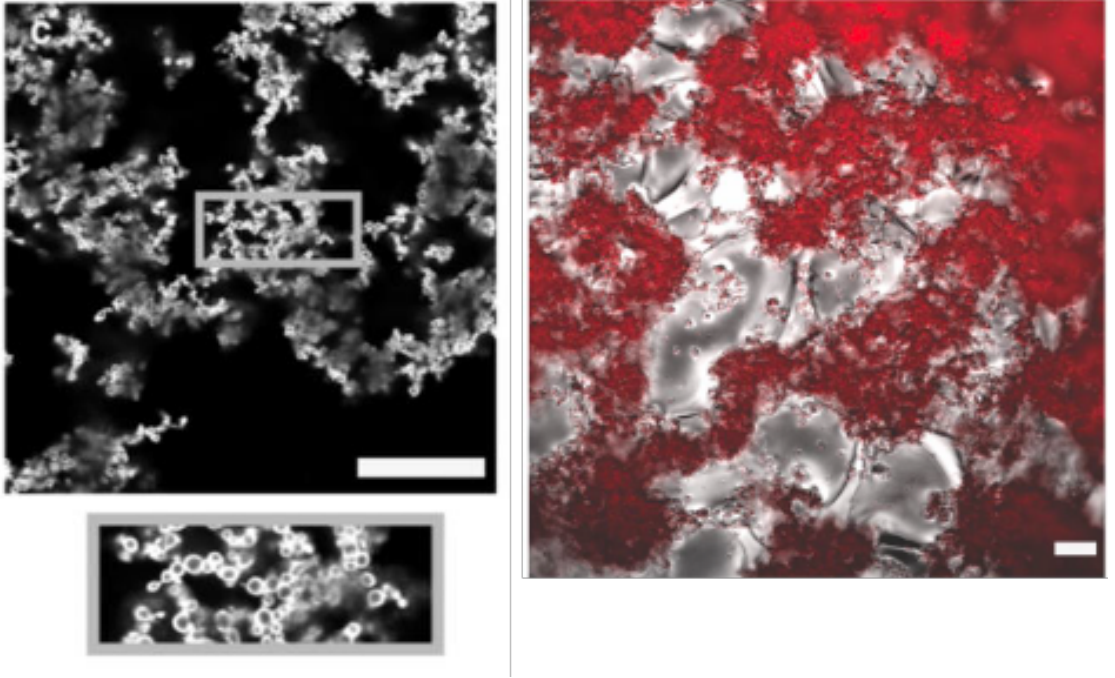
Figure 3.4: a) Fluorescence confocal tile scan images of an aggregate formed at quench depth c) $\Delta T = 30°$C (scale bar 20μm) at 0.30 wt% concentration of ligand modified QDs in 5CB liquid crystal, with enlarged high lightened insets showing colloid chaining feature. b) Overlaid fluorescence microscopy image (red) of an aggregate (quench depth $\Delta T = 35°$C, 0.45 wt% QDs in 5CB liquid crystal), with the corresponding birefringence image using crossed polarizers to highlight defect lines in the nematic phase (scale bar 100μm).

vent, [84] we expect the mechanism of attraction to be different in liquid crystal where colloids are subject to a quadrupolar attractive potential [85,86]. The chaining motifs we observed on short length-scales compare well with previous observations by Muševič [6]. The chains prominent in Figure 3.4a are most likely due to interacting topological defects around the colloids [3,87] but similar configurations can also occur when colloids decorate existing line defects in nematic liquid crystal. Unfortunately, we were unable to distinguish between these mechanisms for many specific chains because the crowded three-dimensional nature of the aggregates made imaging of individual defects close to the colloids difficult, especially in cases where the colloids were about 1–2μm in diameter.

A close examination of the system after aggregation revealed that there are many liquid crystal line defects throughout the nematic phase which remain after

the initial defect annihilation stage of nematic phase formation. These defect lines wrap around and stretch between colloids in the aggregate (Figure 3.4). These residual nematic line defects seem to play a role in overall aggregate stabilization.

3.4.3 Aging of aggregate
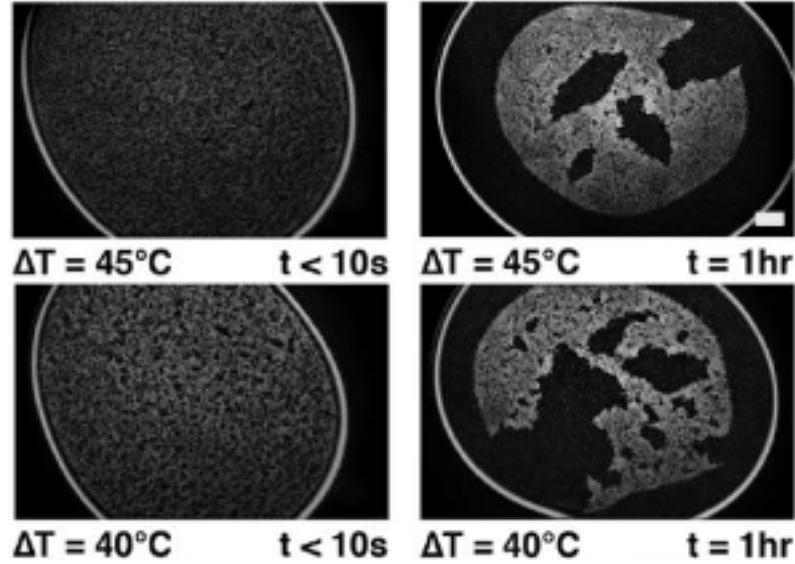
Figure 3.5: Fluorescence microscopy images taken 1hr apart at different ΔTs for QD concentration of 0.15wt% for all three aggregates. Scale bar = 100μm.

In addition to the colloidal motion driven by individual mutual attractions, we observed occasional larger-scale aging events which have a significant impact on the final aggregate structure. We observed many instances of local rearrangement of colloids, shrinkage, breaking of colloidal strands and opening of large voids in the aggregate structure. Once open, these new voids increase in size. A typical event occurs when two large clusters are attached by a bridging nematic line defect, or chain of colloids. The chain is under tension and appears to break, opening a void in the aggregate as the large clusters continue to shrink and move apart. Clear evidence of this phenomena is shown in Figure 3.5, where fluorescence microscope images of four different aggregates are pictured after 10s and 1h, demonstrating the appearance of voids. At t = 10s, the aggregates appear fairly homogenous on length scales > 100μm. After 1h, the structures have changed significantly, with a

decrease in volume and voids of various sizes present. Void formation events can be identified using the spatial velocity autocorrelation function (Figure 3.9) where anticorrelations (negative values for $\psi(r)$) at larger r can be interpreted as the result of clusters separating after connecting chain breakage.

3.4.4 Aggregate morphology as a function of quench depth and concentration of quantum dots in liquid crystal
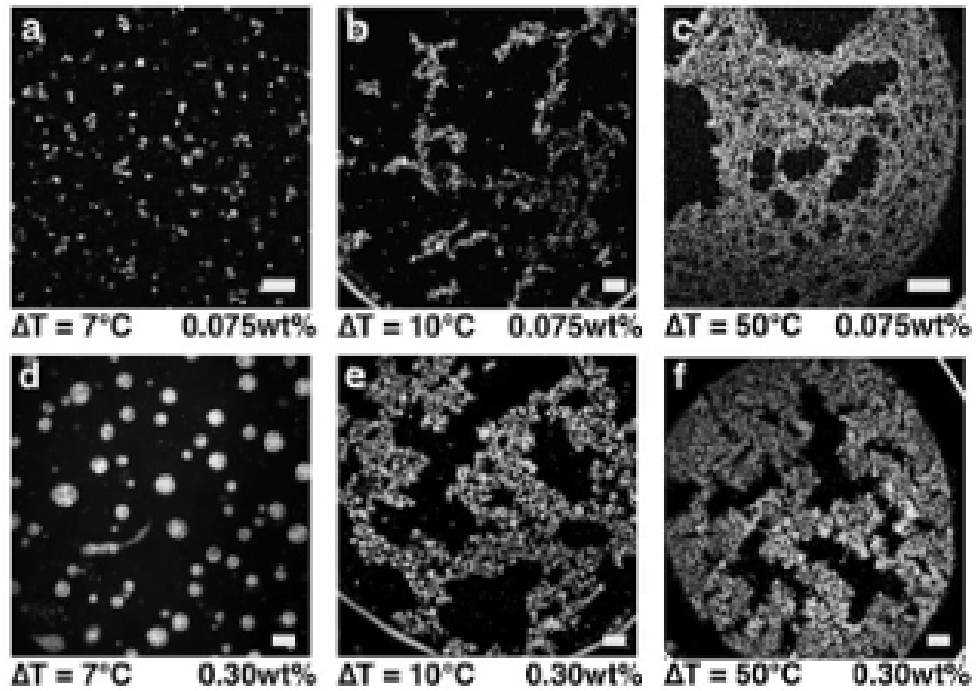
Figure 3.6: Fluorescence microscopy images of different aggregate morphologies (a-f), formed at different ΔTs and QD concentrations.

Figure 3.6 highlights a range of aggregate structures that form depending on initial quantum dot concentration and temperature quench depth. These two parameters have been shown to control colloid size and number density [22]. At lower colloid number densities (Figure 3.6a) the system does not aggregate into a single object, instead form local clusters. If we increase colloid density in different samples, the aggregates change from tenuous fractals with a web-like appearance,

to percolating networks and then fill into a more gel-like dense structure at high density.

3.4.5 Quantification of aggregate structure and aging using pair auto-correlation function

To quantify the structure of the aggregates we calculated the pair auto-correlation function, $g(r)$ in quasi-equilibrium, 24hrs after formation (Figure 3.7a), and at different times in the aggregation process to quantify structural changes (Figure 3.8). Figure 3.7a shows a log-log plot of the pair auto-correlation function $g(r)$ for three representative aggregates formed at different quench depths. The results were close to linear, as expected for a fractal aggregate. The slope of each curve in the linear region was found to be 1.49, 1.41 and 1.43 for $\Delta T = 20°C$, $\Delta T = 25°C$ and $\Delta T = 30°C$ respectively. The peak at short length-scale (indicated using arrows), in each curve is characteristic of the average colloid–colloid separation. Using this peak, we estimated average colloid size for the three quenches to be $d = 12.59\mu m \pm 0.62$, $d = 5.01\mu m \pm 0.56$ and $d = 1.58\mu m \pm 0.52$ for $\Delta T = 20°C$, $\Delta T = 25°C$ and $\Delta T = 30°C$ respectively. We compared these results to manual measurements of the average colloid size using the ImageJ measurement tool and found excellent consistency (Figure 3.7b). The data in Figure 3.7b was fitted to a power law $\xi \sim \Delta T^d$ where d was estimated to be 4.5 ± 0.1. While this result was qualitatively consistent with previous findings of ref [22], however the strength of the fitting function was quite surprising. Thus, indicating the relationship between colloid size and quench depth needs further elucidation and cannot be described by a simple power law. Other features in the $g(r)$ curve at longer length-scales can be attributed to a characteristic cluster/void size in the aggregates.

We calculated $g(r)$ curves as a function of time in one typical aggregate ($\Delta T = 20°C$) to quantify colloid distribution over time (Figure 3.8). At t = 0s we first see a curve consistent with a random distribution of particles [32–34], confirming the initial state of the system immediately after the colloids are formed. After the quench, the colloids form under 1s. From 20-80s we can see the colloids have started to move towards each other and the lowest point of $g(r)$ increases, until
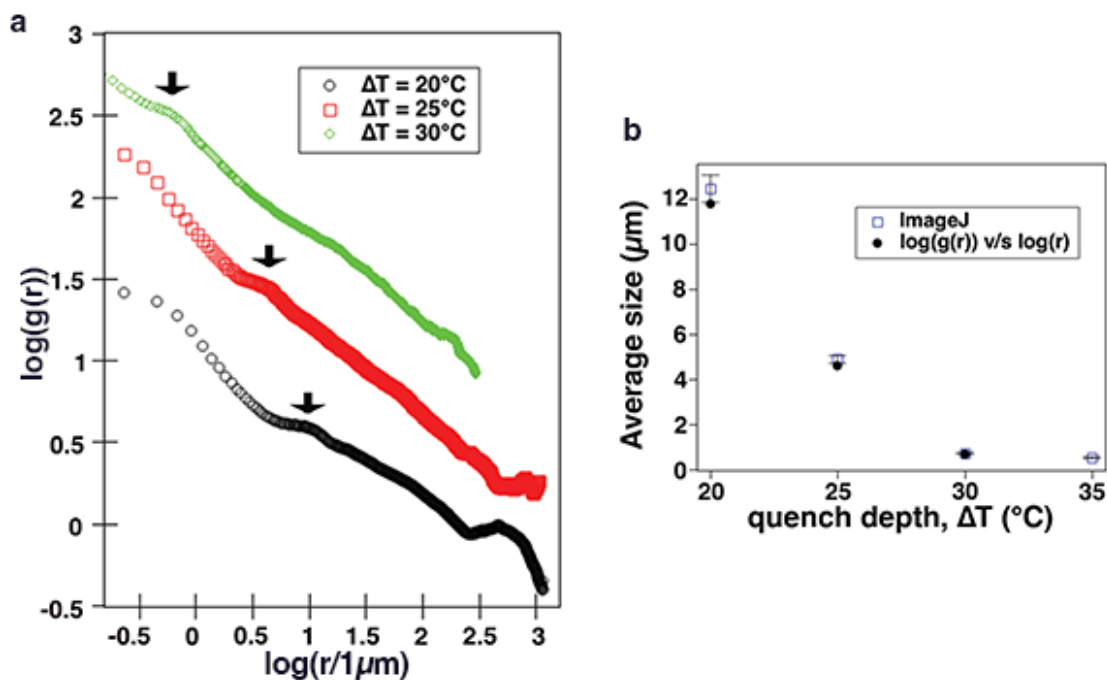
Figure 3.7: a) Log plot of pair auto-correlation function for aggregates formed at different Ts for a concentration of 0.15wt%. b) Colloidal size as a function of ΔT.

120s when a shoulder appears on the curve. This small peak is characteristic of a well-defined nearest-neighbor separation in the system, and thus we can assume chains have begun to form. At later times the peak washes out and $g(r)$ tends towards the linear slope, more characteristic of an aggregate. The cartoons next to Figure 3.8 illustrate the short-range change in $g(r)$ with time. At early times colloids have no nearest neighbors, and we see a deep dip in $g(r)$. Later, after chain formation, on the shortest length-scales, there is a significant chance of nearest neighbor separations over a well-defined distance defined by the chain packing. At later times the aggregate has compacted further, and the chain motif is less dominant producing a wider range of nearest neighbor separations. At later times (15–33 min) aging events such as breakage of colloidal strands, void formation, and continued compaction also occur, impacting the overall structure and $g(r)$ leading to the quasi-equilibrium structure described earlier in this section.
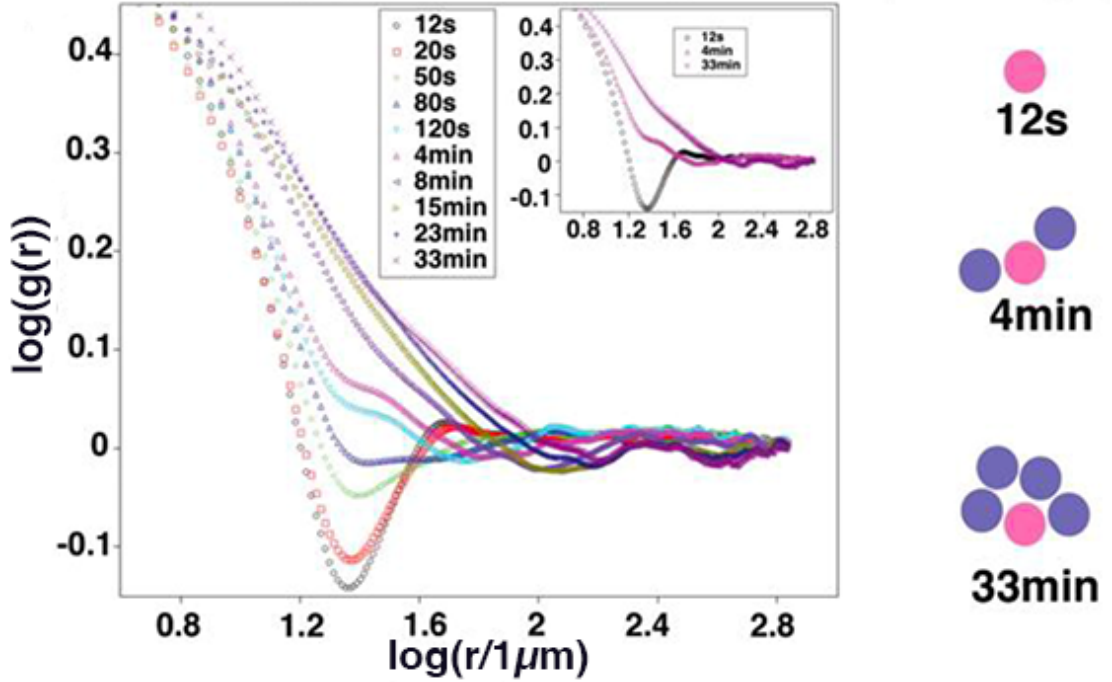
Figure 3.8: Time evolution of log of $g(r)$ during 33mins of aggregation for $\Delta T = 20°C$ and nanoparticle concentration of 0.15wt% with an accompanying cartoon to demonstrate the increase in nearest neighbors with time.

3.4.6 Velocity autocorrelation function (VACF) analysis of colloidal aggregation and aging in liquid crystal

We calculated the spatial velocity autocorrelation function (VACF) to gain insights into the dynamics of colloidal motion during aggregation and ageing. It is complementary to the mass correlation function $g(r)$ (Figure 3.8) described in the above section. Initially following a temperature quench, colloids move individually and then in small groups as clusters begin to form. This early-stage behavior can be seen in the time window 0-119s. Velocity correlations drop rapidly over 0-100μm. Particles within the same cluster will have highly correlated velocities and the growth of the clusters is reflected in the increase in the VACF curves to higher r with time. At later times in the analysis, we also observe that $\psi(r)$ becomes negative, indicating some tendency for the largest clusters to move in opposite directions. This anti-correlation can be explained by considering the breakage events that happen during aging. When large shrinking clusters connected by a
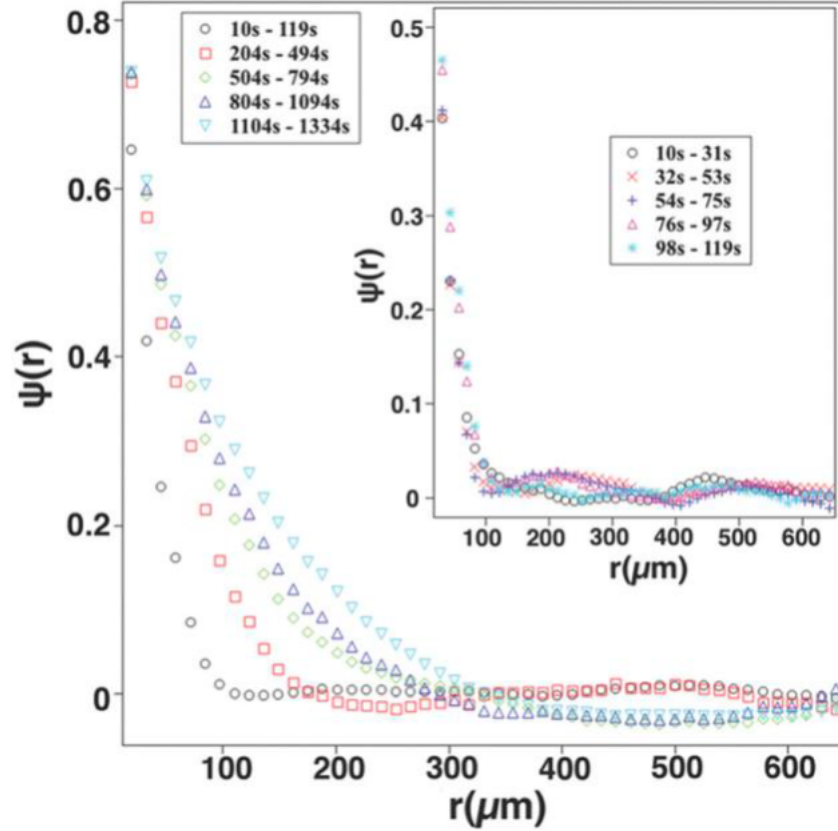
Figure 3.9: VACF calculated for different time windows for ΔT=20°C and 0.30wt% nanoparticle concentration in 5CB.

few colloids separate and move apart, they open up a void in the gel.

3.5   Conclusion

In summary, we developed a novel method to achieve large-scale aggregation of micron-sized colloidal particles in the liquid crystal nematic phase. For this, we took advantage of a recently developed one-pot synthesis method designed to form well-dispersed luminescent colloids *in situ* in the nematic phase. This method is unique in producing a random initial colloidal distribution in the liquid crystal without the need for additional particle dispersion steps such as external mixing or sonication that could influence the final aggregate structure. Colloid sizes are controlled by temperature quench depth through the isotropic to nematic transi-

tion, at which point the colloids self-assemble. We used fluorescence microscopy to characterize aggregate structures with varying colloid size and density. The observed structures range from dense gels to more tenuous fractal aggregates and isolated clusters. Using optical observations and spatial correlation functions we found that aggregation proceeds first via mutual colloidal interactions driven by Frank elasticity, then there are important contributions from defect annealing and compaction which produce dramatic ageing effects after initial aggregate formation, in particular the appearance of large internal voids.

Spherical colloids when placed into a liquid crystal phase increase the free energy of the system by distorting the director field. When colloidal capsules used in this work are formed after a temperature quench, each colloid is accompanied by a pair of topological defects known as boojums and it is energetically cost-effective to share defects, hence colloids group together and organize into chains [85] and decorate line defects formed at the phase transition. As time progresses some defects annihilate, while others are wrapped around and stretched between clusters, holding the aggregate structure together. In Wood et al. [88] molecular dynamics simulations showed that Saturn-ring defects on neighboring particles can merge to form entangled point defects, giving rise to clusters of a few particles, some of which can be linear or planar. These clusters interact and hold each other in place through long-range elastic distortions in the LC. Our results are very consistent with these findings and provide additional evidence that large scale gels can be stabilized by entangled topological defects.

In general, the aggregate compacts to reduce the overall free energy via local colloidal rearrangements and defect annealing events. The signatures of these events are evident both from microscopic observations and our quantification of structure dynamics. We can conclude that initial aggregation proceeds via a cluster–cluster aggregation process to form a loose network of colloid chains. Then, local compaction and annealing events lead to the emergence of voids in the aggregate.

Unlike in isotropic solvents, for which there are several widely known growth models including diffusion limited cluster aggregation (DLCA) [89], predicting the

detailed structure and dynamics of large-scale aggregation and gelation of colloids in liquid crystal is a much more complex problem. In particular, as the clusters grow the three-dimensional nematic director field around the growing colloid clusters changes continually. Plus, the presence of colloid-trapping line defects and loops makes this a particularly intractable theoretical problem. For anisotropic solvents such as a nematic liquid crystal, no similar comprehensive growth models exist and our research suggests that there is a need for a new Elasticity Limited Cluster Aggregation (ELCA) model, applicable to anisotropic fluids, in which concepts important in liquid crystal physics such as Frank elasticity and topological defects determine the final colloidal gel structure.

Chapter 4

Behavior of chemically powered Janus colloids in lyotropic chromonic liquid crystal

In this chapter, I discuss the development of a non-biological active nematic by combining the passive nematic liquid crystal with artificial micro-swimmers. For this we chose an aqueous based lyotropic chromonic liquid crystal, disodium cromoglycate (DSCG), with nematic phase at room temperature. This host phase was doped with Janus colloids fabricated with platinum (Pt) - capped polystyrene (PS) spheres, that exhibit self-propelled motion in hydrogen peroxide (H_2O_2) solutions via its catalytic decomposition into water and oxygen. Through meticulous control of experimental parameters, we achieved directed motion of Pt-coated Janus particles in DSCG. This is the first observation of chemically powered active Janus particles moving in a liquid crystal environment. Our examination of individual Janus colloids moving in a uniformly aligned nematic phase of DSCG, using fluorescence and polarized microscopy video imaging, revealed some surprising behaviors. The particle motion is governed by liquid crystal anisotropy, but also strongly influenced by asymmetries in the individual particles. The Janus colloids move approximately parallel to the direction of nematic orientation defined by the director. Motion analysis over a range of timescales indicate a cross-over from ballistic to super-diffusive behavior on timescales below the relaxation time

for liquid crystal elastic distortions. In addition, non-uniformities in metallic cap coatings and fuel distribution around the colloid have non-trivial effects on particle propulsion direction and anomalous rolling behaviors.

4.1   Introduction

Active fluids are out-of-equilibrium systems composed of active elements (particles, rods etc.) suspended in a fluid medium. These active elements transduce energy from their environment into autonomous motion, causing the fluid to exhibit rich dynamic behavior. Such behavior can include collective motion [28, 90, 91], motility-induced phase separation [92, 93], flow instabilities, and pattern formation [94–96]. Several recent studies have focused on the behavior of active particles dispersed in isotropic fluids, including self-assembly and their collective dynamics [29–31]. A relatively unexplored direction in this field, concerns the replacement of the suspending fluid by a non-Newtonian anisotropic fluid, a nematic liquid crystal. Liquid crystals (LCs) are elastic fluids with some degree of anisotropy. They have long-range molecular orientational order, described by the director, $\hat{n}$. When a spherical colloid is immersed in a uniformly aligned nematic LC, it will locally perturb the nematic director field as determined by the particle surface anchoring [7, 51, 86]. The anisotropic viscosity and Frank elasticity [4, 35, 86] make LCs an interesting environment to study the motion of active colloids.

For this work, we chose chemically powered synthetic active Janus colloids driven by a surface chemical reaction. Common propulsion mechanisms of these colloids include self-diffusiophoresis or self-electrophoresis [33, 65, 66]. We used Janus colloids fabricated with platinum (Pt) - capped polystyrene (PS) spheres, that exhibit self-propelled motion in aqueous hydrogen peroxide (H_2O_2) solution via catalytic decomposition of H_2O_2 into water and oxygen. The liquid crystal host in our experiments, was carefully selected as disodium cromoglycate (DSCG), a chromonic lyotropic liquid crystal with a nematic phase at room temperature [57, 97]. This material provides an aqueous environment compatible with the hydrogen peroxide powered Janus particles. DSCG was recently used to in-

vestigate the motion of bacteria in liquid crystal, where experiments showed the preferred direction of propulsion was parallel to the director [32]. Remarkably, at very low bacterial concentrations, Zhou et al. [32] introduced a novel class of active matter – the living liquid crystal – induced by the activity of bacteria moving in passive liquid crystal. These living liquid crystals, exhibit chaotic dynamics and motile topological defects, which are strikingly similar to the dynamic characteristics of microtubule-based active nematics [98]. Inspired by these results, we focused on studying the behavior of individual active Janus particles in a nematic liquid crystal, as a synthetic analog to the bacterial system [32]. Elucidating the fundamentals of Janus particle motion in a liquid crystal environment represents the first step towards studying their collective motion.

In our experiments, DSCG was aligned by treating the bounding glass substrates with polyimide SE-7511, to give a planar director orientation [99]. This configuration allowed easy observation of particle position and orientation using fluorescence and polarized optical microscopy. Visualization using crossed polarizers and full wave retardation plate, revealed the liquid crystal distortion profiles around the particles. Tracking the motion of active Janus colloids showed that liquid crystal anisotropy significantly influenced their trajectories. Particles tended to move close to the direction of average molecular ordering defined by the director. Our analyses reveal that motion profiles are characterized by a combination of anomalous diffusion and ballistic behavior. We also observed the Janus colloids rolling while moving in DSCG, despite no significant change in their direction of motion.

4.2   Experimental methods

4.2.1   Janus colloid preparation

Janus colloids were prepared by coating polystyrene microspheres with metallic platinum (Pt) using electron beam (e-beam) deposition. Polystyrene fluorescent microspheres (FPM-4056-2 (4μm spheres, Nile red) and FCM-10052-2 (11.8μm spheres, Yellow), Spherotech, Inc.) were selected as the base particles. Before
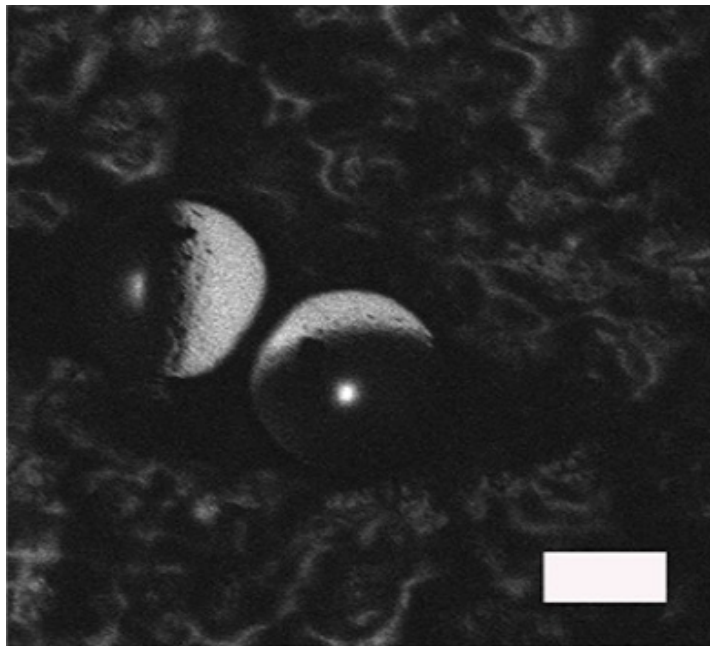
Figure 4.1: SEM image, captured with backscattered electron detection mode, of 4μm sized fluorescent microspheres (excitation 510nm, emission 550nm) half coated with Pt. Scale bar = 2μm.

coating the colloids with a metal layer, they were first diluted in ethanol and then spread evenly on a glass slide. Once dried, the colloids were coated by e-beam deposition with 3nm of Nickel (Ni) followed by 30 nm of Pt. The Ni layer was added to make the colloids magnetic to potentially explore how magnetic torques would affect the colloids' behavior, although such experiments were not part of the current study. After coating, the non-metallic hemisphere of the particle remained fluorescent. The colloids were then removed from the slide using a small piece of wet lens tissue gently dragged over the slide to pick up the colloids. The tissue was then placed in a plastic 1.5mL tube containing approximately 0.5mL of de-ionized water and the tube was shaken and vortexed before removing the tissue. The finished particles were characterized using scanning electron microscopy (SEM) with a ZEISS Gemini SEM 500 instrument. Figure 4.1 shows an SEM image of two particles, the conductive hemisphere (lighter) is clearly visible for each (scale bar = 2μm).

4.2.2 Liquid crystal cell preparation
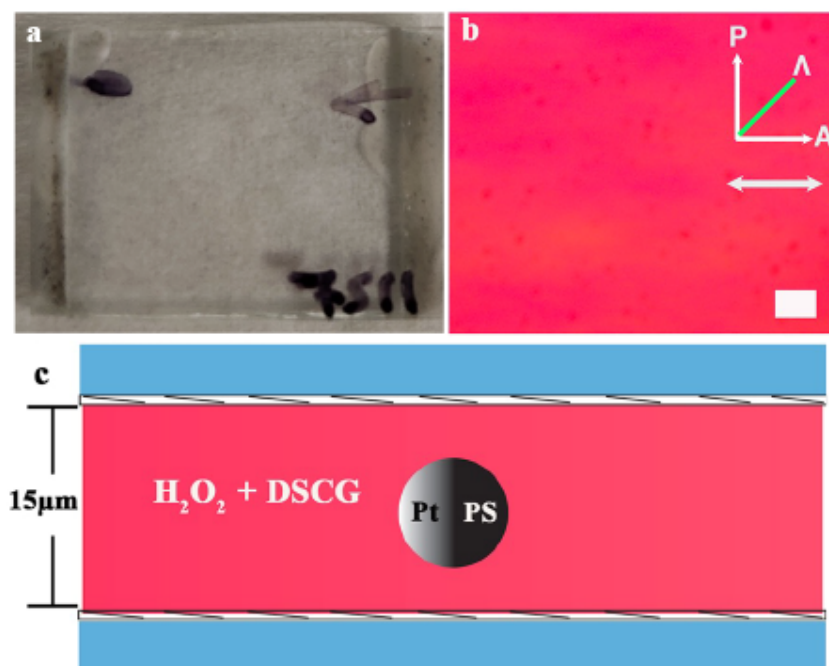
Figure 4.2: a) Assembled cell of thickness 15μm. b) Polarized microscopy image of uniformly aligned DSCG inside an assembled cell. Imaged using a full wave (λ) retardation plate, as indicated by the green line. Polarizer (**P**) and Analyzer (**A**) directions are also indicated. Scale bar = 2μm. c) Cross-sectional schematic of the experimental cell containing DSCG, H$_2$O$_2$ and a Janus particle.

We worked with two different Janus colloid diameters, 4.0μm and 11.8μm. From a stock solution containing colloids of each respective size, 5μL was pipetted and re-suspended in 30% H$_2$O$_2$ aqueous solution. After this dilution the new solution now has a H$_2$O$_2$ concentration of 20%. This solution was then sonicated before mixing with liquid crystal. The Pt coating on the particle is quite reactive, generating significant O2 bubbles. This is a problem especially for the larger particles. The bubbles make colloid visualization difficult and form many air-liquid interfaces that influence particle trajectories. Therefore, we aimed to minimize their production. To do so for each particle size, we optimized the wait time after the initial addition of H$_2$O$_2$ solution to the particle suspension - 1hr for the 4.0μm Janus colloids and 3hrs for the 11.8μm Janus colloids. After these respective wait times, 1μL of a control particle solution (polystyrene divinylbenzene, DVB spheres 6μm diameter,

0.5 mg/mL) was also added to the Janus/ H_2O_2 solutions.

A dispersion of 25wt% DSCG (Sigma Aldrich) in de-ionized water was prepared, then subsequently diluted to 15.38wt% (to be in the nematic phase) by adding $5\mu L$ of the prepared Janus/ H_2O_2 solution. This method produced a final 7.21% concentration of H_2O_2, enough for activity, while minimizing oxygen bubbles. To further minimize the effect of bubbles causing advective flows, the Janus + DSCG + fuel solution was loaded into the pre-assembled cell after an additional waiting time. One hour for the $4\mu m$ Janus colloids and 6hrs for the $11.8\mu m$ colloids. The cell was constructed from two parallel glass plates (20mm x 10mm) separated by $15\mu m$ spacers. The interior surfaces of the glass plates were pre-treated with polyimide SE-7511 [99] and rubbed with a velvet cloth to produce unidirectional planar anchoring. The cells were assembled by putting together pairs of substrates with rubbing directions being antiparallel to each other (Figure 4.2a). Figure 4.2b shows an optical microscope image of a uniformly aligned cell filled with DSCG. After loading, the cell was sealed with epoxy glue and placed flat on the microscope stage to minimize gravitational effects due to tilt. Proper cell sealing and placement on the stage are important to minimize drift during imaging. The absence of drift was verified using DVB control spheres. The loaded cells were imaged with polarized optical microscopy (POM) using a Leica DM2500P upright microscope with a HI PLAN 40x/0.65 objective lens. Videos were recorded at 1 frame per second over a period of 8min using a color camera [Basler Ace 2.3MP]. Figure 4.2c shows a diagram of the experimental cell.

4.2.3   Particle tracking and Image analysis

Janus colloids were tracked spatially from fluorescence microscopy images using Trackpy – a python package which locates Gaussian blob-like features in video images, follows them through time and records their trajectories [100]. Tracking yields x, y coordinates for each colloid as a function of i, the frame number. The liquid crystal was imaged between crossed polarizers with a full wave retardation plate. Figure 4.2b, shows an example image of an aligned DSCG nematic phase with the director, polarizer and retardation plate directions indicated.

4.3   Analysis techniques

4.3.1   Length of distortions ("twisted tails")

Colloidal particles suspended in DSCG are 'dressed' by chiral distortions called twisted tails by the surrounding nematic director. We used crossed-polarized microscopy images to calculate the twisted tail lengths associated with 4μm 11.8μm Janus colloids (Figure 4.3). Prior to calculation, the images were converted into 8-bit. As demonstrated in the supplemental material of [101] intensity profile was plotted for a line along the equatorial plane of the Janus colloid. The resulting decaying intensity tails were fitted with the Gaussian peak equation,

$$I = I_0 + \frac{A}{w}\sqrt{\frac{2}{\pi}}\exp\left(-2\left(\frac{x-x_c}{w}\right)^2\right) \tag{4.1}$$

and the length was estimated using the Full Width at Half Maximum (FWHM) concept. In the above equation, the width parameter w is related to the standard deviation σ, by $\sigma = \frac{w}{2}$. This gives a FWHM $= \sqrt{2\ln 2}w$ representing the length of intensity spread around the colloid. We take the average of the decaying intensity tails on the two sides to find the tail length.

4.3.2   Mean squared displacement (MSD) analysis

MSD curves for each individual particle track, defined by {x(i), y(i)} were calculated using the method described in reference [102]. The MSD, for a given time lag t, is defined as the average over all pairs of points separated by that time lag using,

$$\langle \Delta r^2(t)\rangle = \frac{\sum_{i=1}^{N_i}[(x(t_i+t)-x(t_i))^2 + (y(t_i+t)-y(t_i))^2]}{N_i} \tag{4.2}$$

In this definition, t_i is the time for the ith image in the track and N_i represents the number of images over which the average is calculated.

4.3.3   Intensity analysis

The fluorescence microscopy videos show a bright feature (the fluorescent side of the Janus colloid) moving in time against a black background. To characterize

the orientation of the colloid we took advantage of the fact that only one hemisphere (the non-metallic side) is fluorescent. By observing a single particle, the total integrated intensity in every video frame was obtained using Trackpy [100]. Maximum intensity in this case corresponds to a full moon configuration – when the metallic cap is facing down, and the fluorescently labelled polystyrene half is facing up. A minimum intensity corresponds to a new moon configuration – when the metallic cap is facing up and the fluorescently labelled polystyrene half is facing down. To normalize these integrated intensities, the intensity of each frame in a video was divided by (I_{max}), the maximum observed integrated intensity.

4.3.4 $\Delta\theta$ analysis

To measure how much the direction of motion of active colloid deviates from the nematic director orientation, we calculated $\Delta\theta = \Delta\theta_{LC} - tan^{-1}(\frac{dy}{dx})$ where $\Delta\theta_{LC}$ is the nematic director orientation (in our experiments it is 45°) and dx, dy are the displacements of active Janus moving in liquid crystal along x, y directions respectively.

4.4   Results

4.4.1   Director distortions around Janus colloids

When a colloidal particle with well-defined surface anchoring is introduced in a uniform director field, the interplay of elastic and surface anchoring forces defines the director configuration surrounding the colloid [3]. The inherent asymmetry and distinct surface properties of Janus colloids result in unique interactions with surrounding nematic, leading to novel and varied distortions in the director field. We used POM imaging to investigate the nature and scale of nematic distortions around the colloid. The different Janus configurations discussed here are i) full-moon – where the Pt metallic cap on one side is facing down, maximum brightness; ii) half-moon – where both sides of the Janus are showing, half bright, and iii) new-moon – where the metallic cap is facing up, minimum brightness. Figure 4.3 (a-c)
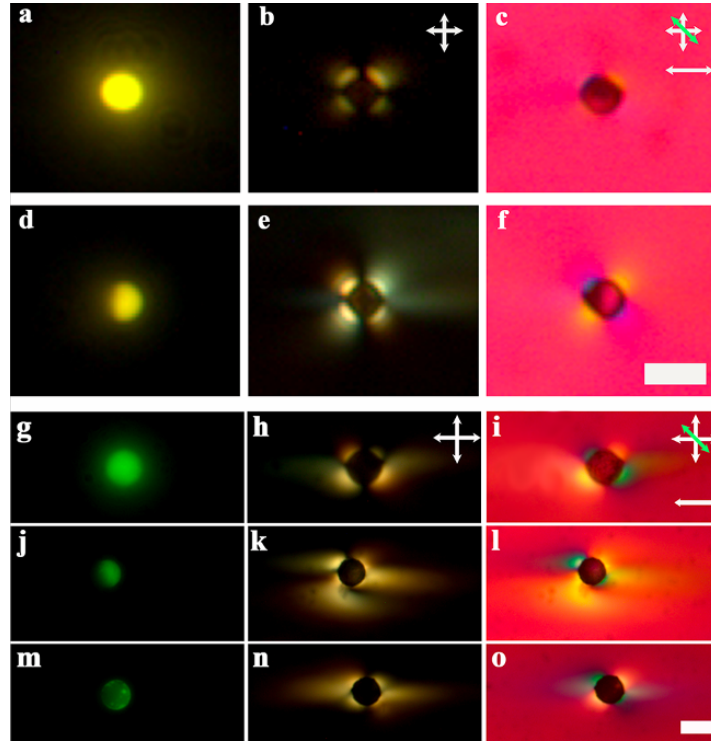
Figure 4.3: Microscope images of 4μm Janus particle inside 18μm thick cell in full moon (a,b,c,) and half-moon (d,e,f) configurations under different imaging modes. a,d) Fluorescence microscopy images. b,e) crossed-polarized microscopy images. c,f) crossed polarized microscopy images with an inserted full wave retardation plate (green arrow shows the slow axis). Scale bar = 5μm. Microscopy images of 11.8μm Janus particle inside 30μm thick cell in full moon (g,h,i), half-moon (j,k,l) and new moon (m,n,o) configurations under different imaging modes. g,j,m) Fluorescence microscopy images. h,k,n) crossed-polarized microscopy images. i,l,o) crossed-polarized microscopy images with an inserted full wave retardation plate (green arrow). Scale bar =10μm. Magnification 63x water immersion, NA = 0.9

shows a 4μm diameter Janus colloid in the full moon configuration imaged under three different modes. The POM image (Figure 4.3b) shows a weakly distorted nematic around the colloid. But close observation by inserting a full-wave retardation plate between the crossed polarizers (Figure 4.3c) reveal slight yellow tinges around the particle, signaling that the nematic distortions on each side of the colloid are locally chiral. This chiral nature becomes a little more obvious in the half-moon configuration (Figure 4.3(d-f)). As large colloids with similar anchoring cause longer-range distortions in the nematic director, making optical observations

easier, we see the same local chirality with 11.8μm diameter Janus colloid (Figure 4.3(g-o)). Similar chiral distortions were observed by A. T. Martínez et al [101] with passive DVB spheres having tangential surface anchoring in the same liquid crystal. These distortions are characterized by "twisted tails" that extend away from the particle parallel to the far-field nematic director. This behavior can be understood because DSCG has an unusually small twist elastic modulus making twist distortions energetically cheap [57]. Unlike in conventional LCs, where spherical particles with tangential anchoring give quadrupolar distortions with large splay and bend distortions in the surrounding nematic. In DSCG the director twists, reducing the energies of splay and bend. This twist has handedness rendering chirality to the distortion. The type of twisted tail director configuration we see around the colloid (Figure 4.3) is called class-1. In a class-1 configuration symmetry, the director spirals around the central axis in the same sense on opposite sides of the colloid. The director configuration resembles a chiral dipole, characterized as an elastic multipole with both quadrupolar and chiral dipolar terms. These results suggest that, despite the Janus particle's inherently different hemispherical sides, anchoring around the colloid is overall tangential, albeit with different anchoring strengths between hemispheres as indicated by unequal tail lengths on both hemispheres.

We quantified the twisted tail lengths for the particles in Figure 4.3 using the Full Width at Half Maximum (FWHM) concept described in [101]. For the 4μm Janus particle in full-moon, the distortions were too weak to identify the intensity spread along the equatorial plane. Comparatively, for the half-moon, the tail lengths were $\sim 5.65\mu$m and unequal, with the Pt side being longer. Similarly, for the 11.8μm Janus particle, the tail lengths were $\sim 30.00\mu$m, 43.51μm and 41.84μm for the full-moon, half-moon and new-moon configurations respectively, with the Pt side consistently longer. The tail length can increase with particle size (consistent with the results of [101]) and vary with the orientation of the Janus particle.
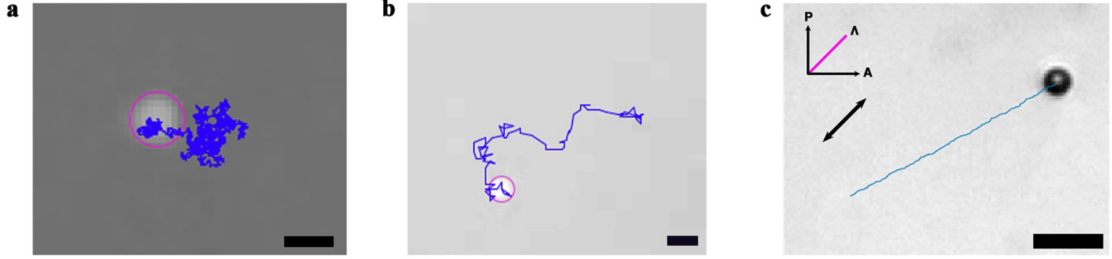
Figure 4.4: a) Trajectory of an inactive Janus colloid in water recorded for 5mins at 50fps. Scale bar = 5μm b) Trajectory of an active Janus colloid in 7.21% H2O2 solution captured for a duration of 10min at 0.2fps. Scale bar = 5μm. c) Trajectory of an active Janus colloid in DSCG inside an aligned pre-assembled cell recorded for 8min at 1fps. Scale bar = 10μm.

4.4.2 Motion of active Janus in DSCG

To understand the role of liquid crystal in dictating the motion of active Janus particles we performed a series of experiments. First, we studied their behavior in water under two different scenarios, 1) without any fuel, 2) with fuel (7.21% peroxide solution). With no fuel, the Janus colloids exhibit characteristic Brownian motion (Figure 4.4a). In the presence of fuel, the Janus colloids become active and exhibit enhanced Brownian motion with a directional component to their motion, (Figure 4.4b). The results of these control experiments were compared with motion in the nematic phase of DSCG in the presence of fuel (7.21% peroxide concentration), (Figure 4.4c). When introduced in an uniaxially aligned liquid crystal, in the presence of fuel, the Janus colloids show ballistic behavior. Figure 4.4c, show an active Janus colloid self-propel in a direction slightly close to that of the nematic director. The overall motion of active Janus particle in DSCG can be explained by considering the interplay between the particle's intrinsic propulsion mechanisms, anisotropic viscous interactions with the director field and hydrodynamic effects. To understand this, let's consider an axis $\mathbf{J}$ which is the polar axis of the Janus particle and an axis $\mathbf{N}$ which is the axis of the director field around the colloid (a line connecting the "tails"). Propulsion along the overall director is expected because of the viscous anisotropy of DSCG. As follows from the measurements of the diffusion constants for Brownian motion of colloidal spheres [103], the ratio $\sigma_{\parallel}/\sigma_{\perp}$
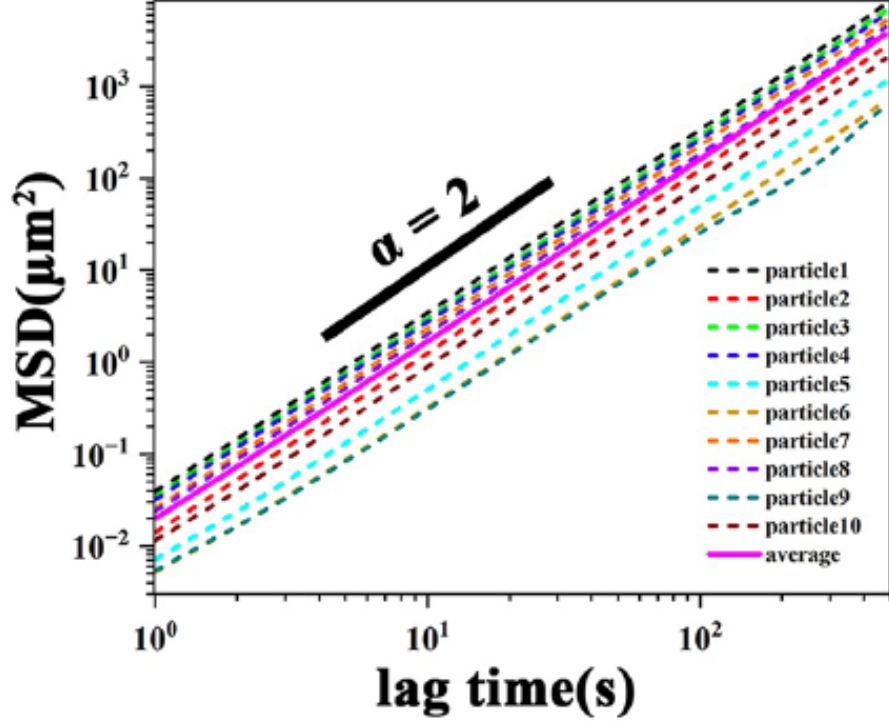
Figure 4.5: Mean squared displacement (MSD) plots on a logarithmic scale, of individual active Janus colloids moving in uniformly aligned DSCG inside a cell of thickness 15μm and captured at 1fps for 8min

of the effective viscosity $\sigma_\parallel$ for displacements along the director to the viscosity $\sigma_\perp$ for perpendicular displacements is significantly smaller than 1, $\sigma_\parallel/\sigma_\perp = 0.66$. But when the **J** axis rotates away from the **N** axis because of the propulsion forces generated by the particle and the hydrodynamic flows around the particle, lateral displacements from the director occur. The restoring elastic force arising from the distorted director field tend to align the particle's motion with the director. The nature of active Janus particle trajectory is discussed in detail in section 4.4.5. This is the first report of chemically powered synthetic Janus particles moving in a liquid crystal environment. Motion profiles of the Janus particles were analyzed by plotting the mean square displacement (MSD) of the particles as a function of time. Figure 4.5 shows MSD plots for 10 different 4μm-diameter active Janus particles (represented by dotted lines) moving in DSCG. The particles were each tracked for 8min at 1 frame per second (fps) and their motion plotted on a log-

log scale. The solid magenta line represents the average of all 10 trajectories. A linear fit to this average produces a slope of 1.98 ± 0.01 indicating that motion is predominantly ballistic throughout the time of observation. Within a lag time of 480s (period of observation), 4μm diameter Janus particles were observed to travel distances ranging from 24μm – 90μm. These differences are likely due to variation in the amount of fuel around different particles. Once the Pt + H_2O_2 reaction fuel fully depletes, the Janus particles behave like passive colloids.

4.4.3 Anisotropic and anomalous motion of active Janus colloids

To investigate the directional preference of a single active Janus colloid, we calculated MSDs parallel and perpendicular to the director. MSDs, averaged over 10 active Janus colloids, clearly show that motion parallel to the far-field director is substantially longer than motion perpendicular to the director (Figure 4.6a). We can understand this behavior by considering the anchoring around the colloids which causes asymmetric director field distortions (Figure 4.3) and an effective anisotropic viscosity. When 'dressed' by the surrounding director field, the Janus particle suspended in DSCG effectively becomes an anisotropic twisted composite object, with different effective viscosities for motion parallel and perpendicular to the director. Such viscoelastic effects have been shown to favor particle displacement along the director [103]. In our case, due to misalignment of the $\mathbf{J}$ and $\mathbf{N}$ axes, we did observe some translation perpendicular to the director. But $\mathrm{MSD}_\parallel$ is significantly larger than $\mathrm{MSD}_\perp$.

In addition to their anisotropic motion over long timescales, we also observed that the colloids exhibit anomalous diffusion when the time step between the measurement of particle position was 0.05s. In this experiment, five different active Janus colloids (4μm in diameter) moving in DSCG inside a cell of thickness 15μm were recorded for 5mins at time steps of 0.05s. Trajectories for analysis were obtained by splitting the 5min long video into tracks of duration 1min. A time averaged MSD calculation was performed on each 1min track. Then an ensemble average was taken by averaging over these 1min trajectories. As Janus particles
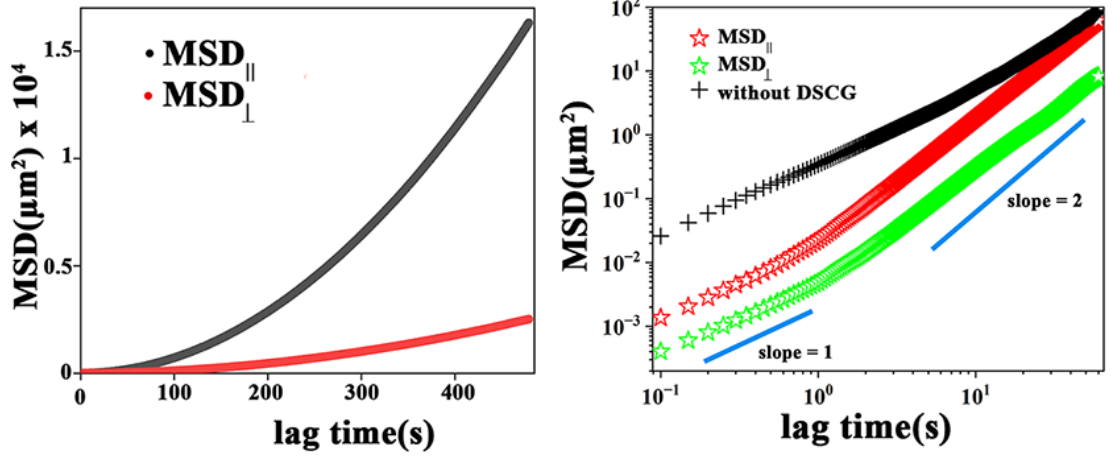
Figure 4.6: MSD plots calculated parallel and perpendicular to the director, averaged over 10 different active Janus colloids moving in DSCG inside an aligned cell of thickness 15μm, captured for 8min at 1fps. b) MSD plots of active Janus colloids in the presence and absence of DSCG recorded for 1min at 20fps.

are moving in an anisotropic environment, motion parallel and perpendicular to the director were calculated separately (Figure 4.6b). The MSD curves reveal two regimes of motion – a regime with a smaller slope at short lag times that slowly transitions into a steeper slope at longer lag times. The crossover time for MSD$_{\parallel}$ corresponds to t$_{\parallel}$ = 0.79s with a slope of 1.14 $\pm$ 0.02 at t < t$_{\parallel}$ and 1.95 $\pm$ 0.01 at t > t$_{\parallel}$. The crossover time for MSD$_{\perp}$ is at t$_{\perp}$= 1.39s with a slope of 1.09 $\pm$ 0.01 at t < t$_{\perp}$ and 1.85 $\pm$ 0.01 at t > t$_{\perp}$. However, the same MSD curve calculated in water (with H$_2$O$_2$ but no liquid crystal), showed no crossover between slopes (Figure 4.6b black crosses). When a particle moves in a nematic liquid crystal, it distorts the director field and the associated velocity field. The coupling between the particle's motion and the fields, combined with the inherent fluctuations in the director field, introduces an intrinsic memory effect, where past disturbances influence the particle's subsequent behavior. As the particle moves, it creates perturbations in the director which relax over a characteristic time $\tau \sim \frac{\eta l^2}{K}$, where l is the characteristic length of the director distortion relaxing back to equilibrium, η is the rotational viscosity, which we estimated to be $\sim$ 0.2Pa.s [104] and K is the Frank elastic constant. These dynamic interactions and the continuous influence of the memory effect result in anomalous diffusion. Assuming $l = 1\mu$m for

the class 1, active Pt- coated Janus sphere with a configuration specific distortion profile and twist elastic constant of DSCG at 23°C [57], τ was found to be ~ 0.29s. This τ value is slightly less than the crossover time, below which anomalous diffusive behavior was observed. Turiv et al [103] reported sub-diffusive behavior for tangentially anchored inactive silica spheres in DSCG with crossover times 0.37s and 0.46s for motion parallel and perpendicular to the director, respectively. In our case, we observe a slight super-diffusive behavior. This is because of activity affecting particle dynamics at short time scale.

Moreover, our report of crossover time for motion perpendicular to the director is different from A. T. Martínez et al [101]. In ref [101], the examined particles are away in the bulk, in our case they are close to the substrate. When particles are close to the substrate the memory span of fluctuating deformations in the surrounding nematic is strongly affected by the cell thickness. The lifespan of fluctuations is written as $\tau_h \approx \frac{\eta_{\text{eff}} h^2}{K \pi^2}$ where h is the thickness of the cell [103]. For our cell of thickness 15μm $\tau_h \sim 3$s, which is slightly above the time we observe anomalous behavior for motion parallel and perpendicular to the director.

4.4.4 Small-sized active Janus particle rolls showing "moon phases"

The 4μm Janus particle undergoes rolling, exhibiting different moon phases (Figure 4.7), with the intensity graph showing peaks and valleys. A peak corresponds to a full moon configuration and a valley indicate a new moon configuration. Before discussing these results, it is important to consider possible mechanisms for particle rolling.

Active particles move via self-generated phoretic mechanisms in the presence of fuel and the motion occurs in general, due to the interaction of self-generated fields with the interfacial boundary region of the particle. The particle/liquid crystal interfacial boundary layer is a very thin region of the surrounding fluid much less than the size of the particle. The self-generated field around the particle can consist of a solute concentration gradient, set up by the catalytic chemical reaction on the Pt side, or an electric field generated by proton currents at the Pt end that emanate
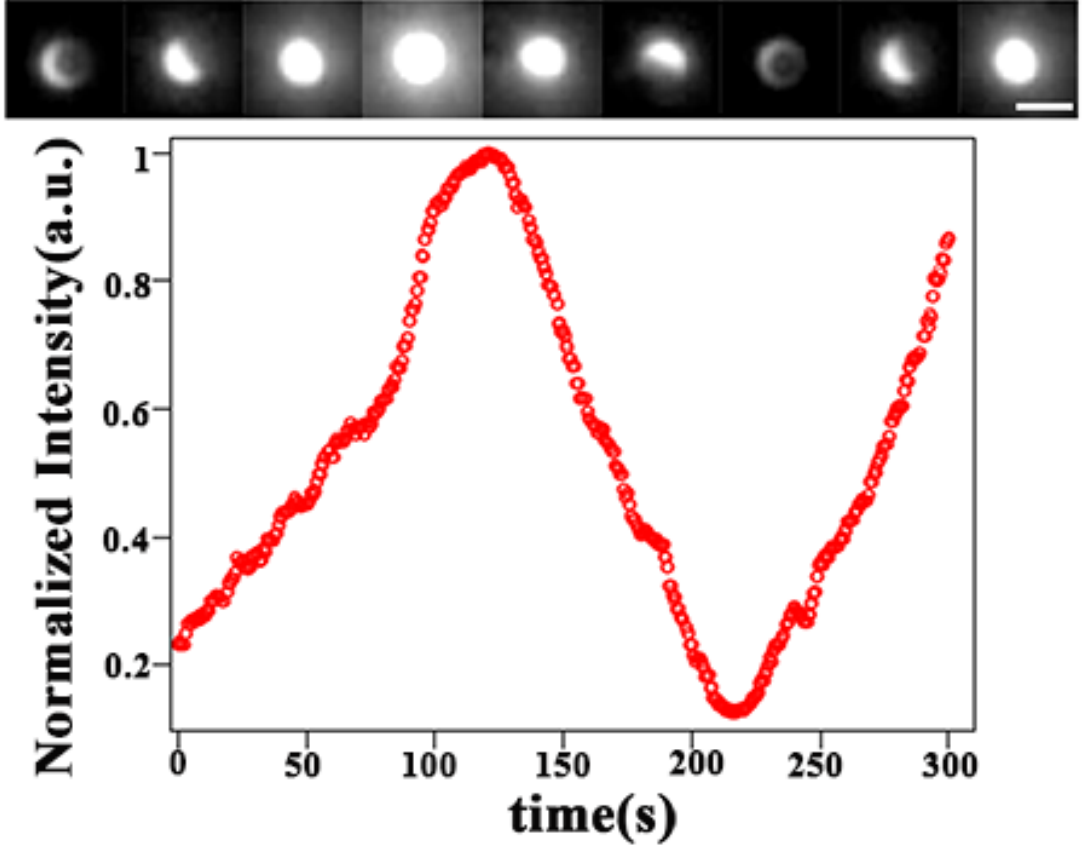
Figure 4.7: Fluorescence microscopy images capturing the moon phases of a 4μm active Janus particle inside a 18μm cell for a duration of 5min and corresponding intensity plots of the of the same Janus particle demonstrating rolling. Scale bar $= 5\mu$m.

from the vicinity of the equator and end near the pole [67]. These fields create a local pressure imbalance leading to an effective slip velocity along the interfacial boundary layer, driving fluid flows [66, 105–107]. The self-phoretic effective slip velocity, v_s, induced by the solute concentration field, C, along the interface can be written as $v_s = \mu\nabla_{\parallel}C_s$ [105]. Here, μ is the characteristic diffusiophoretic mobility and $\nabla_{\parallel}C_s$ is the tangential gradient of C at the outer limit of the boundary layer. While considering self-propulsion through electrokinetic effects, μ is replaced with the zeta potential, ζ and C with a self-generated electric field, ψ [107]. Any spatial non-uniformity in the mobility constant caused by fabrication defects, can lead to a rotational component of the effective slip velocity. The particle velocity will

be proportional to the sum of the mobilities, and angular velocity is proportional to the difference between the mobilities on the two sides [108]. We expect the particle to turn and align its axis of symmetry along the field gradient. This would mean that after adopting this configuration (for example PS side first), rolling should cease. In our case we observe something different. The particles continue to rotate throughout their tracked trajectories, and do not reach an orientational equilibrium (Figure 4.8a). To try to explain this phenomenon, we can consider the effects of a spatially varying fuel concentration field. Such a variation would add polar and azimuthal components to the local slip velocities at the particle surface, greatly complicating determination of the particle mobility [107, 108].

4.4.5 Curvature in trajectory, not a perfect straight line

In water (Figure 4.4b), Janus particles can exhibit spiral trajectories, due to their non-uniform surface properties. The non-uniformity in surface coating creates an off-center propulsive force, which produces a torque that leads to spiraling behavior [64, 109]. When active Janus particles are placed in an aligned liquid crystal their hydrodynamic interactions with the nematic are likely to be of the pusher type, which forces fluid outward along their swimming direction and draw fluid into the sides of their bodies. This behavior, as described in the theoretical model by Lintuvouri et al [110] leads to particles swimming parallel to the nematic director due to the hydrodynamic coupling between their flow field and the anisotropic viscosities of the liquid crystal. In this context, the off-center propulsive force generated by the non-uniform surface coating causes the particles to deviate from a straight path. Meanwhile, the elastic restoring force from the liquid crystal environment counteracts this deviation, guiding the particles back towards a linear propulsion direction aligned with the nematic director. The net effect leads to a slightly curved trajectory, or linear propulsion in a direction slightly different to the nematic director. In Figure 4.8a, we can see a Janus particle moving in aligned DSCG, with the nematic director indicated by a double headed arrow. The particle begins its path in the half-moon configuration, then rolls to adopt a full moon configuration and continues forward. The corresponding deviation in
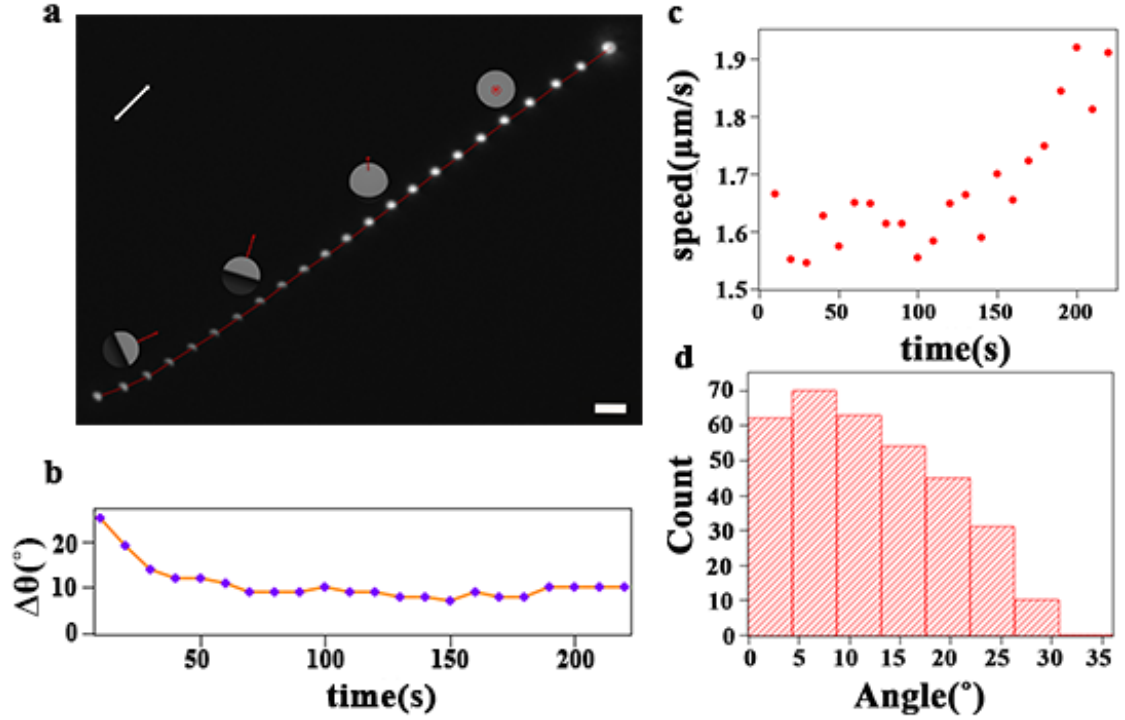
Figure 4.8: a) Composite image showing the curved trajectory of a rolling 4μm Janus particle inside a 15μm DSCG cell, captured every 10s for 220s with the **J** vector indicated as a red arrow, Scale bar $=10\mu$m. b) Graph of $\Delta\theta$, the deviation in direction of motion with respect to the nematic director orientation, c) speed, with time for the particle depicted in (a). d) Histogram of $\Delta\theta$ values that active 4μm Janus particles take while moving in DSCG observed for a duration of 220s at every 10s interval, calculated for seven different particles.

particle trajectory with respect to the nematic director ($\Delta\theta$) is plotted in Figure 4.8b. While in the half-moon configuration, $\Delta\theta$ is high, then the particle rolls, and $\Delta\theta$ drops to $\sim 10°$. We observe a rise in velocity (Figure 4.8c) as the Janus particle trajectory comes more in alignment with the nematic director. Figure 4.8d shows a histogram of $\Delta\theta$s calculated for 7 different active Janus particle trajectories. The most common trajectory direction, $\Delta\theta$ was in the range 4.4°- 8.8°. As particles move in DSCG, we typically observe some curvature in their trajectories – they don't always move in a straight line while propelling close to the director orientation. This behavior is very non-intuitive, based on the simplified picture of Janus particle propulsion. It should be noted that the behavior of each Janus particle moving in DSCG is, to some extent, unique. Although general behaviors

can be obtained, the surface chemical properties of each particle can vary from spot to spot. Adding to this, possible spatial non-uniformity of the fuel environment around the colloid, makes each Janus particle different. In addition to these local effects, global inhomogeneities in the fuel concentration field further complicate the behavior. Under these conditions, rolling behavior can be considered stochastic over long timescales.

4.4.6 Active Janus particle rolls and yet undergo no change in direction of motion

In Figure 4.8a, we see a fascinating result - the particle rolls with no change in its direction of motion. Considering that particle propulsion occurs in general due to catalytic breakdown of H_2O_2 on the particle's Pt side [33, 66–68], there are two important things to note. First, surface chemical activity – how quickly a concentration gradient can be set-up by the chemical reaction and second, the surface phoretic mobility – how effectively the surface interacts with this gradient to generate fluid flows [64]. S. Ebbens et al. [67] reported particle motion as a combination of neutral and ionic diffusiophoresis as well as electrophoretic effects whose interplay can be varied through ionic effects such as pH and salt concentration. DSCG is a disodium salt and high salt concentrations are known to reduce the turnover rate of H_2O_2 [67]. The characteristic diffusion time of reaction products (O_2, H_3O^+) around the Janus colloid (4μm) is gives as $\tau_d = \frac{R^2}{D}$, where $D = \frac{k_B T}{6\pi\eta a}$, which depends on the rotational viscosity of DSCG and the radius of the product particle, a [111]. For O_2 and H_3O^+ $\tau_d \sim 0.55$s and 0.37s respectively. These calculated values for τ_d and our observation timescale for the colloid to change direction suggest that while the rotational configuration of the Janus takes time to react to the fuel and set-up a gradient, the existing gradient may give enough thrust to push the particle forward.

4.4.7   Large Janus colloids don't roll

Finally, we observed the large colloids (11.8μm in diameter) don't roll while moving in DSCG, (Figure 4b) and tend to move in a direction closer to the director. This can be understood as they create a larger elastic distortion in the surrounding director field (Figure 4.3), and in general move much more slowly. In addition, because their distortion profiles are sensitive to particle orientation, rolling for larger particles becomes increasingly energetically expensive.

This behavior might also be related to elastic levitation as described by O. P. Pishnyak et al [36] where elastic repulsion from the bounding substrates keeps the colloid in the nematic bulk, mediated by director distortions. A large colloid is repelled more strongly from the substrates than a small colloid, thus a larger colloid is often levitating near the mid-plane of the cell. This positioning reduces the shear stress differences above and below the colloid and therefore suppresses rolling.

Colloidal particles in liquid crystal cells are known to interact elastically with the bounding plates [36, 112]. The gap between the spherical surface of a Janus sphere and the flat plates above and below it forms a double-wedge geometry, which induces director gradients. With tangential anchoring at the colloid and planar anchoring at the plate, the only region where the director is not distorted is along the line that connects the bottom and the top of the Janus sphere to the neighboring plate; other regions elastically adjust to the tilt of the colloidal surface with respect to the plates. The director gradients become stronger as the particle approaches a flat plate, which means that the sphere is elastically repelled from the plate [36,112]. The repulsion is stronger for larger particles [112]. Experiments with two homeotropically anchored spheres, one large and one small, demonstrate that the larger particle "levitates" closer to the mid-plane of the cell as compared to a smaller particle, which finds itself closer to the bounding plate [56]. The reason is that the elastic repulsion force grows as r^4 with the radius r of the colloid [36, 112], which is faster than the gravity force proportional to r^3. We expect a similar effect for the tangentially anchored colloids, since the repulsive force between two quadrupolar colloids scales as r^6 [113–115] and the sphere-plate
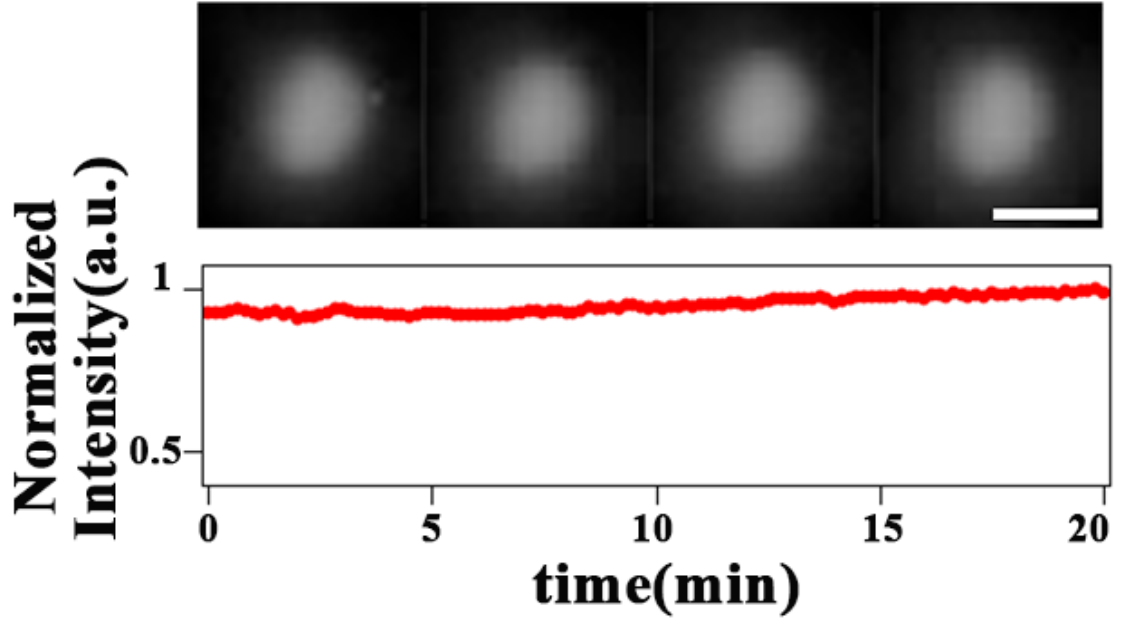
Figure 4.9: Fluorescence microscopy images of 11.8μm active Janus particle inside a 30μm cell recorded over a duration of 20min and corresponding intensity plot demonstrating the absence of rolling over the period of observation. Scale bar = 10μm.

repulsion can be modeled as an interaction of a colloid with its mirror image [18]. Since the smaller colloid is likely to be displaced from the midplane of the cell by gravity, one expects an inverse of the Quincke effect observed for colloids moving in a liquid crystal [39, 40]. Namely, in the Quincke effect, an electrically driven rotation of a sphere results in its translation when it is not strictly in the midplane of the cell because of the hydrodynamic interactions with the boundaries [39, 40]. In our case, the self-propelled translating colloid is expected to rotate because of the difference between the hydrodynamic interaction with the top and bottom plates; thus, the inverse Quincke effect.

4.5   Conclusion

In summary, we developed a method to achieve directed movement of synthetic, chemically powered active Janus particles in a liquid crystal nematic phase. On observing individual particle trajectories, we found that particle motion is governed

by the liquid crystal anisotropy but is also strongly influenced by asymmetries in the individual particles. Motion is ballistic over longer timescales and is influenced by orientation-dependent director distortions around the particle. In addition, non-uniformities in metallic cap coatings and fuel concentration lead to non-trivial effects on particle propulsion direction and anomalous rolling behaviors. By studying the basic behaviors of anisotropic fluid on single Janus colloids my work helps to lay the foundation for developing novel active matter systems based on synthetic subunits.

Chapter 5

Future directions

In this thesis, we described the underlying mechanisms behind large-scale colloidal aggregation and the subsequent structure development in liquid crystal solvents, highlighting the importance of understanding the complex interactions driven by Frank elasticity relaxation and the role of topological defects. We also investigated the directed movement of synthetic, chemically powered active Janus particles in a nematic liquid crystal phase emphasizing how liquid crystal anisotropy and particle asymmetry govern their motion. This work lays the foundation for developing novel active matter systems based on synthetic subunits.

I would like to conduct additional experiments to test our conjectures regarding the anomalous rolling behaviors of the Janus particles. I plan to use optical microscopy to study the influence of unequal shear stresses on the top and bottom sides of the Janus particles by finding their positions inside the liquid crystal cell, relative to the top and bottom bounding plates. I would also like to perform further experiments on the motion of active Janus particles in water to examine how the addition of salts affects their direction of motion. This will help interpret why active Janus particles roll without changing their direction of motion in DSCG.

Zhou et al. [32] reported the onset of collective behavior at a remarkably low volume fraction, close to 0.2%, of active bacteria moving in DSCG. I'm interested in finding the critical concentration of Pt-coated Janus particles and H_2O_2 required to achieve "the living liquid crystal state", exhibiting dynamic effects similar to that of active microtubule bundles [98]. Use polarized optical microscopy to track

the transition from individual states to complex patterns, analyze defects, and calculate velocity vector field and velocity auto-correlation function using particle image velocimetry analysis to find the active length scale [116].
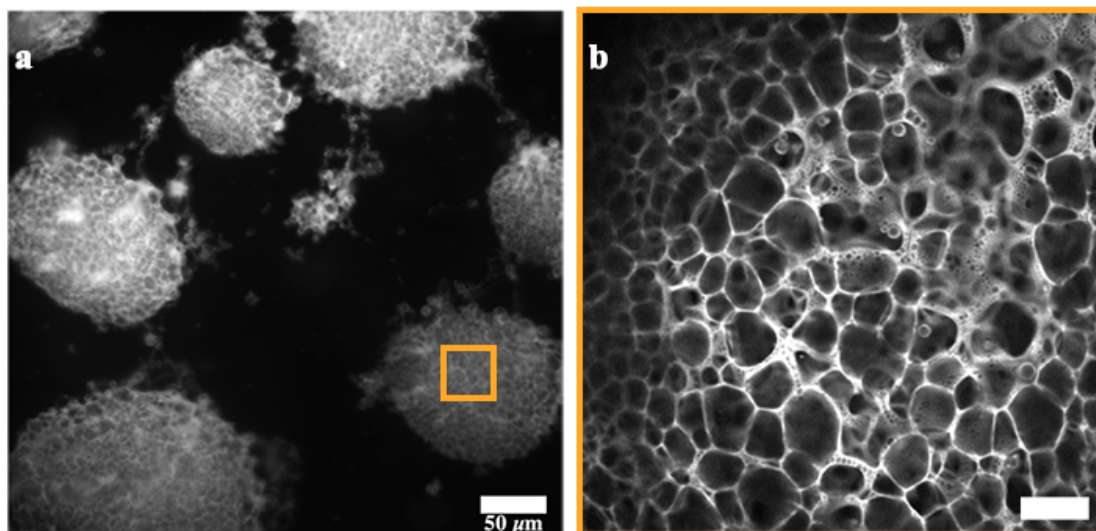
Figure 5.1: a) Fluorescence microscopy image of foam morphology formed by re-cooling an aggregate structure made with a QD concentration of 0.30wt% and quench depth $\Delta T = 30°C$ through the same quench depth. Scale bar $= 50\mu$m. b) Zooming in one of the foam blobs show a dense packing of polygonal cells. Scale bar $= 10\mu$m.

In addition to the aggregation project, I'm also interested in understanding shapeshifting morphologies in liquid crystal. By subjecting the quasi-equilibrium aggregate structure to a cycle of heating and cooling, we can induce its irreversible transformation into a foam-like morphology. My focus is on studying this phenomenon through the lens of liquid-liquid phase separation. I aim to explain the reorganization process and the final stability of the structure based on entropy, interaction energy, and interfacial surface tension. I have completed the experimental procedures and confocal imaging for this project. Now, in collaboration with Dr Timothy Atherton at Tufts University, we are working on simulations utilizing Morpho software [117] to elucidate structural details of this elastic foam.

Bibliography

[1] Paul C Hiemenz and Raj Rajagopalan. *Principles of Colloid and Surface Chemistry, revised and expanded*. CRC press, 2016.

[2] Duncan J Shaw and IT. *Introduction to colloid and surface chemistry*, volume 123. Butterworths London, 1970.

[3] Igor Muševič. *Liquid crystal colloids*, volume 530. Springer, 2017.

[4] Holger Stark. Physics of colloidal dispersions in nematic liquid crystals. *Physics Reports*, 351(6):387–474, 2001.

[5] Ivan I Smalyukh, OD Lavrentovich, AN Kuzmin, AV Kachynski, and PN Prasad. Elasticity-mediated self-organization and colloidal interactions of solid spheres with tangential anchoring in a nematic liquid crystal. *Physical review letters*, 95(15):157801, 2005.

[6] Igor Musevic, Miha Skarabot, Uros Tkalec, Miha Ravnik, and Slobodan Zumer. Two-dimensional nematic colloidal crystals self-assembled by topological defects. *Science*, 313(5789):954–958, 2006.

[7] Philippe Poulin, Holger Stark, TC Lubensky, and DA Weitz. Novel colloidal interactions in anisotropic fluids. *Science*, 275(5307):1770–1773, 1997.

[8] Jean-Christophe Loudet, Philippe Barois, and Philippe Poulin. Colloidal ordering from phase separation in a liquid-crystalline continuous phase. *Nature*, 407(6804):611–613, 2000.

[9] Ph Poulin and DA Weitz. Inverted and multiple nematic emulsions. *Physical Review E*, 57(1):626, 1998.

[10] Martin Zapotocky, Laurence Ramos, Philippe Poulin, TC Lubensky, and DA Weitz. Particle-stabilized defect gel in cholesteric liquid crystals. *Science*, 283(5399):209–212, 1999.

[11] Qingkun Liu, Ye Yuan, and Ivan I Smalyukh. Electrically and optically tunable plasmonic guest–host liquid crystals with long-range ordered nanoparticles. *Nano letters*, 14(7):4071–4077, 2014.

[12] Yuan Zhang, Qingkun Liu, Haridas Mundoor, Ye Yuan, and Ivan I Smalyukh. Metal nanoparticle dispersion, alignment, and assembly in nematic liquid crystals for applications in switchable plasmonic color filters and e-polarizers. *Acs Nano*, 9(3):3097–3108, 2015.

[13] S Umadevi, Xiang Feng, and Torsten Hegmann. Large area self-assembly of nematic liquid-crystal-functionalized gold nanorods. *Advanced Functional Materials*, 23(11):1393–1403, 2013.

[14] Javad Mirzaei, Mitya Reznikov, and Torsten Hegmann. Quantum dots as liquid crystal dopants. *Journal of Materials Chemistry*, 22(42):22350–22365, 2012.

[15] MA Shahzamanian and S Shoarinejad. Dynamics of two colloidal particles immersed in a nematic liquid crystal. *Journal of Physics: Condensed Matter*, 19(15):156101, 2007.

[16] M Tasinkevych, NM Silvestre, and MM Telo Da Gama. Liquid crystal boojum-colloids. *New journal of physics*, 14(7):073030, 2012.

[17] Aurora D González-Martínez, Marco A Chávez-Rojo, Edward J Sambriski, and José A Moreno-Razo. Defect-mediated colloidal interactions in a nematic-phase discotic solvent. *RSC advances*, 9(57):33413–33427, 2019.

[18] G Foffano, Juho S Lintuvuori, A Tiribocchi, and D Marenduzzo. The dynamics of colloidal intrusions in liquid crystals: A simulation perspective. *Liquid Crystals Reviews*, 2(1):1–27, 2014.

[19] Paul Meakin. Diffusion-limited aggregation in three dimensions: results from a new cluster-cluster aggregation model. *Journal of colloid and interface science*, 102(2):491–504, 1984.

[20] DA Weitz, JS Huang, MY Lin, and J Sung. Limits of the fractal dimension for irreversible kinetic aggregation of gold colloids. *Physical review letters*, 54(13):1416, 1985.

[21] Swetlana Jungblut, Jan-Ole Joswig, and Alexander Eychmüller. Diffusion- and reaction-limited cluster aggregation revisited. *Physical Chemistry Chemical Physics*, 21(10):5723–5729, 2019.

[22] Sheida T Riahinasab, Amir Keshavarz, Charles N Melton, Ahmed Elbaradei, Gabrielle I Warren, Robin LB Selinger, Benjamin J Stokes, and Linda S Hirst. Nanoparticle-based hollow microstructures formed by two-stage nematic nucleation and phase separation. *Nature Communications*, 10(1):894, 2019.

[23] Andrea L Rodarte, Blessing H Cao, Harmanpreet Panesar, Ronald J Pandolfi, Makiko Quint, Lauren Edwards, Sayantani Ghosh, Jason E Hein, and Linda S Hirst. Self-assembled nanoparticle micro-shells templated by liquid crystal sorting. *Soft Matter*, 11(9):1701–1707, 2015.

[24] VJ Anderson, EM Terentjev, SP Meeker, J Crain, and WCK Poon. Cellular solid behaviour of liquid crystal colloids 1. phase separation and morphology. *The European Physical Journal E*, 4(1):11–20, 2001.

[25] VJ Anderson and EM Terentjev. Cellular solid behaviour of liquid crystal colloids 2. mechanical properties. *The European Physical Journal E*, 4(1):21–28, 2001.

[26] Peter G Petrov and Eugene M Terentjev. Formation of cellular solid in liquid crystal colloids. *Langmuir*, 17(10):2942–2949, 2001.

[27] Iain D Couzin, Jens Krause, et al. Self-organization and collective behavior in vertebrates. *Advances in the Study of Behavior*, 32(1):10–1016, 2003.

[28] Tamás Vicsek and Anna Zafeiris. Collective motion. *Physics reports*, 517(3-4):71–140, 2012.

[29] Wei Wang, Wentao Duan, Suzanne Ahmed, Ayusman Sen, and Thomas E Mallouk. From one to many: Dynamic assembly and collective behavior of self-propelled colloidal motors. *Accounts of chemical research*, 48(7):1938–1946, 2015.

[30] Igor S Aranson. Active colloids. *Physics-Uspekhi*, 56(1):79, 2013.

[31] Stewart A Mallory, Chantal Valeriani, and Angelo Cacciuto. An active approach to colloidal self-assembly. *Annual review of physical chemistry*, 69:59–79, 2018.

[32] Shuang Zhou, Andrey Sokolov, Oleg D Lavrentovich, and Igor S Aranson. Living liquid crystals. *PNAS*, 111(4):1265–1270, 2014.

[33] Jonathan R Howse, Richard AL Jones, Anthony J Ryan, Tim Gough, Reza Vafabakhsh, and Ramin Golestanian. Self-motile colloidal particles: from directed propulsion to random walk. *Physical review letters*, 99(4):048102, 2007.

[34] Walter F Paxton, Kevin C Kistler, Christine C Olmeda, Ayusman Sen, Sarah K St. Angelo, Yanyan Cao, Thomas E Mallouk, Paul E Lammert, and Vincent H Crespi. Catalytic nanomotors: autonomous movement of striped nanorods. *Journal of the American Chemical Society*, 126(41):13424–13431, 2004.

[35] Oleg D Lavrentovich. Design of nematic liquid crystals to control microscale dynamics. *Liquid crystals reviews*, 8(2):59–129, 2020.

[36] Oleg P Pishnyak, S Tang, JR Kelly, Sergij V Shiyanovskii, and Oleg D Lavrentovich. Levitation, lift, and bidirectional motion of colloidal particles in an electrically driven nematic liquid crystal. *Physical review letters*, 99(12):127802, 2007.

[37] Oleg P. Pishnyak, Sergij V. Shiyanovskii, and Oleg D. Lavrentovich. Inelastic collisions and anisotropic aggregation of particles in a nematic collider driven by backflow. *Phys. Rev. Lett.*, 106:047801, Jan 2011.

[38] Bohdan Senyuk, Jin-Sheng Wu, and Ivan I. Smalyukh. Out-of-equilibrium interactions and collective locomotion of colloidal spheres with squirming of nematoelastic multipoles. *Proceedings of the National Academy of Sciences*, 121(18):e2322710121, 2024.

[39] Antal Jákli, Bohdan Senyuk, Guangxun Liao, and Oleg D. Lavrentovich. Colloidal micromotor in smectic a liquid crystal driven by dc electric field. *Soft Matter*, 4:2471–2474, 2008.

[40] G. Liao, I. I. Smalyukh, J. R. Kelly, O. D. Lavrentovich, and A. Jákli. Electrorotation of colloidal particles in liquid crystals. *Phys. Rev. E*, 72:031704, Sep 2005.

[41] Chenhui Peng, Yubing Guo, Christopher Conklin, Jorge Viñals, Sergij V. Shiyanovskii, Qi-Huo Wei, and Oleg D. Lavrentovich. Liquid crystals with patterned molecular orientation as an electrolytic active medium. *Phys. Rev. E*, 92:052502, Nov 2015.

[42] O Lavrentovich, I Lazo, and O Pishnyak. Nonlinear electrophoresis of dielectric and metal spheres in a nematic liquid crystal. *Nature*, 467:947–950, 2010.

[43] I Lazo, C Peng, J Xiang, Sergij V hiyanovskii, and Oleg D Lavrentovich. Liquid crystal-enabled electro-osmosis through spatial charge separation in distorted regions as a novel mechanism of electrokinetics. *Nat. Comm*, 5:5033, 2014.

[44] Arthur V Straube, Josep M Pagès, Antonio Ortiz-Ambriz, Pietro Tierno, Jordi Ignés-Mullol, and Francesc Sagués. Assembly and transport of nematic colloidal swarms above photo-patterned defects and surfaces. *New Journal of Physics*, 20(7):075006, jul 2018.

[45] S Hernàndez-Navarro, P Tierno, J Ignés-Mullol, and F Sagues. Liquid-crystal enabled electrophoresis: Scenarios for driving and reconfigurable assembling of colloids. *Eur. Phys. J. Spec. Top.*, 224:1263–1273, 2015.

[46] Sergi Hernàndez-Navarro, Pietro Tierno, Jordi Ignés-Mullol, and Francesc Sagués. Ac electrophoresis of microdroplets in anisotropic liquids: transport, assembling and reaction. *Soft Matter*, 9:7999–8004, 2013.

[47] Sergi Hernàndez-Navarro, Pietro Tierno, Joan Anton Farrera, Jordi Ignés-Mullol, and Francesc Sagués. Reconfigurable swarms of nematic colloids controlled by photoactivated surface patterns. *Angewandte Chemie International Edition*, 53(40):10696–10700, 2014.

[48] Devika V S, Dinesh Kumar Sahu, Ravi Kumar Pujala, and Surajit Dhara. Defect-polymorphism-controlled electrophoretic propulsion of anisometric microparticles in a nematic liquid crystal. *Phys. Rev. Appl.*, 18:014030, Jul 2022.

[49] Dinesh Kumar Sahu, Swapnil Kole, Sriram Ramaswamy, and Surajit Dhara. Omnidirectional transport and navigation of janus particles through a nematic liquid crystal film. *Phys. Rev. Res.*, 2:032009, Jul 2020.

[50] Josep M. Pagès, Jordi Ignés-Mullol, and Francesc Sagués. Anomalous diffusion of motile colloids dispersed in liquid crystals. *Phys. Rev. Lett.*, 122:198001, May 2019.

[51] Pierre-Gilles de Gennes and Jacques Prost. *The physics of liquid crystals.* Oxford university press, 1993.

[52] PGa De Gennes. Short range order effects in the isotropic phase of nematics and cholesterics. *Molecular Crystals and Liquid Crystals*, 12(3):193–214, 1971.

[53] Nigel J Mottram and Christopher JP Newton. Introduction to q-tensor theory. *arXiv preprint arXiv:1409.3542*, 2014.

[54] Jonathan V Selinger. *Introduction to the theory of soft matter: from ideal gases to liquid crystals.* Springer, 2016.

[55] John Lydon. Chromonic liquid crystalline phases. *Liquid Crystals*, 38(11-12):1663–1681, 2011.

[56] Suk-Wah Tam-Chang and Liming Huang. Chromonic liquid crystals: properties and applications as functional materials. *Chemical communications*, (17):1957–1967, 2008.

[57] Shuang Zhou. *Lyotropic chromonic liquid crystals: From viscoelastic properties to living liquid crystals.* Springer, 2017.

[58] Ernest G Ehlers. *Optical mineralogy. 1. Theory and technique.* Blackwell, 1987.

[59] PG De Gennes. Phenomenology of short-range-order effects in the isotropic phase of nematic materials. *Physics Letters A*, 30(8):454–455, 1969.

[60] Paul Van der Schoot. Molecular theory of nematic (and other) liquid crystals. *Springer International Publishing*, 1007:978–3, 2022.

[61] Paul M Chaikin, Tom C Lubensky, and Thomas A Witten. *Principles of condensed matter physics*, volume 10. Cambridge university press Cambridge, 1995.

[62] Young-Ki Kim, JungHyun Noh, Karthik Nayani, and Nicholas L Abbott. Soft matter from liquid crystals. *Soft Matter*, 15(35):6913–6929, 2019.

[63] Maurice Kleman and Oleg D Lavrentovich. *Soft matter physics: an introduction.* Springer, 2003.

[64] Brooke W Longbottom and Stefan AF Bon. Improving the engine power of a catalytic janus-sphere micromotor by roughening its surface. *Scientific Reports*, 8(1):4622, 2018.

[65] Krishna Kanti Dey and Ayusman Sen. Chemically propelled molecules and machines. *Journal of the American Chemical Society*, 139(23):7666–7676, 2017.

[66] Jeffrey L Moran and Jonathan D Posner. Phoretic self-propulsion. *Annual Review of Fluid Mechanics*, 49:511–540, 2017.

[67] S Ebbens, DA Gregory, G Dunderdale, JR Howse, Y Ibrahim, TB Liverpool, and R Golestanian. Electrokinetic effects in catalytic platinum-insulator janus swimmers. *Europhysics Letters*, 106(5):58003, 2014.

[68] Aidan Brown and Wilson Poon. Ionic effects in self-propelled pt-coated janus swimmers. *Soft matter*, 10(22):4016–4027, 2014.

[69] Ravi Prasher, William Evans, Paul Meakin, Jacob Fish, Patrick Phelan, and Pawel Keblinski. Effect of aggregation on thermal conduction in colloidal nanofluids. *Applied physics letters*, 89(14), 2006.

[70] Motoyoshi Kobayashi, Frédéric Juillerat, Paolo Galletto, Paul Bowen, and Michal Borkovec. Aggregation and charging of colloidal silica particles: effect of particle size. *Langmuir*, 21(13):5761–5769, 2005.

[71] DA Weitz, MY Lin, and CJ Sandroff. Colloidal aggregation revisited: new insights based on fractal structure and surface-enhanced raman scattering. *Surface Science*, 158(1-3):147–164, 1985.

[72] Linda S Hirst. *Fundamentals of soft matter science.* CRC press, 2019.

[73] MY Lin, H_M Lindsay, DA Weitz, RC Ball, R Klein, and P Meakin. Universality in colloid aggregation. *Nature*, 339(6223):360–362, 1989.

[74] MY Lin, HM Lindsay, DA Weitz, RC Ball, R Klein, and Paul Meakin. Universal reaction-limited colloid aggregation. *Physical review A*, 41(4):2005, 1990.

[75] Thomas A Witten and Leonard M Sander. Diffusion-limited aggregation. *Physical review B*, 27(9):5686, 1983.

[76] H La Roche, JF Fernández, M Octavio, AG Loeser, and CJ Lobb. Diffusion-limited-aggregation model for poisson growth. *Physical Review A*, 44(10):R6185, 1991.

[77] Amir Keshavarz, Sheida T Riahinasab, Linda S Hirst, and Benjamin J Stokes. New promesogenic ligands for host medium microencapsulation by quantum dots via liquid crystal phase transition templating. *ACS Applied Nano Materials*, 2(4):2542–2547, 2019.

[78] Sarah L Veatch, Benjamin B Machta, Sarah A Shelby, Ethan N Chiang, David A Holowka, and Barbara A Baird. Correlation functions quantify super-resolution images and estimate apparent clustering due to overcounting. *PloS one*, 7(2):e31457, 2012.

[79] Prabuddha Sengupta, Tijana Jovanovic-Talisman, Dunja Skoko, Malte Renz, Sarah L Veatch, and Jennifer Lippincott-Schwartz. Probing protein heterogeneity in the plasma membrane using palm and pair correlation analysis. *Nature methods*, 8(11):969–975, 2011.

[80] Sarah L Veatch, Ethan N Chiang, Prabuddha Sengupta, David A Holowka, and Barbara A Baird. Quantitative nanoscale analysis of ige-fcεri clustering and coupling to early signaling proteins. *The journal of physical chemistry B*, 116(23):6923–6935, 2012.

[81] CM Sorensen. The mobility of fractal aggregates: a review. *Aerosol Science and Technology*, 45(7):765–779, 2011.

[82] Eize Stamhuis and William Thielicke. Pivlab–towards user-friendly, affordable and accurate digital particle image velocimetry in matlab. *Journal of open research software*, 2(1):30, 2014.

[83] Kirit N Lad and Arun Pratap. Velocity autocorrelation function for simple liquids and its application to liquid metals and alloys. *Physical Review E—Statistical, Nonlinear, and Soft Matter Physics*, 70(5):051201, 2004.

[84] Andrew I Campbell, Valerie J Anderson, Jeroen S van Duijneveldt, and Paul Bartlett. Dynamical arrest in attractive colloids: The effect of long-range repulsion. *Physical review letters*, 94(20):208301, 2005.

[85] Miha Škarabot, Miha Ravnik, S Žumer, Uroš Tkalec, Igor Poberaj, D Babič, and I Muševič. Hierarchical self-assembly of nematic colloidal superstructures. *Physical Review E—Statistical, Nonlinear, and Soft Matter Physics*, 77(6):061706, 2008.

[86] Ivan I Smalyukh. Liquid crystal colloids. *Annual Review of Condensed Matter Physics*, 9(1):207–226, 2018.

[87] Andrew DeBenedictis, Timothy J Atherton, Andrea L Rodarte, and Linda S Hirst. Modeling deformation and chaining of flexible shells in a nematic solvent with finite elements on an adaptive moving mesh. *Physical Review E*, 97(3):032701, 2018.

[88] Tiffany A Wood, Juho S Lintuvuori, Andrew B Schofield, Davide Marenduzzo, and Wilson CK Poon. A self-quenched defect glass in a colloid-nematic liquid crystal composite. *Science*, 334(6052):79–83, 2011.

[89] Peter J Lu, Emanuela Zaccarelli, Fabio Ciulla, Andrew B Schofield, Francesco Sciortino, and David A Weitz. Gelation of particles with short-range attraction. *Nature*, 453(7194):499–503, 2008.

[90] John Toner, Yuhai Tu, and Sriram Ramaswamy. Hydrodynamics and phases of flocks. *Annals of Physics*, 318(1):170–244, 2005. Special Issue.

[91] Sriram Ramaswamy. The mechanics and statistics of active matter. *Annual Review of Condensed Matter Physics*, 1(Volume 1, 2010):323–345, 2010.

[92] Michael E Cates and Julien Tailleur. Motility-induced phase separation. *Annu. Rev. Condens. Matter Phys.*, 6(1):219–244, 2015.

[93] Clemens Bechinger, Roberto Di Leonardo, Hartmut Löwen, Charles Reichhardt, Giorgio Volpe, and Giovanni Volpe. Active particles in complex and crowded environments. *Reviews of Modern Physics*, 88(4):045006, 2016.

[94] R Aditi Simha and Sriram Ramaswamy. Hydrodynamic fluctuations and instabilities in ordered suspensions of self-propelled particles. *Physical review letters*, 89(5):058101, 2002.

[95] David Saintillan and Michael J Shelley. Instabilities, pattern formation, and mixing in active suspensions. *Physics of Fluids*, 20(12), 2008.

[96] Xiongfei Fu, Lei-Han Tang, Chenli Liu, Jian-Dong Huang, Terence Hwa, and Peter Lenz. Stripe formation in bacterial systems with density-suppressed motility. *Physical review letters*, 108(19):198102, 2012.

[97] Natalie Zimmermann, Gisela Jünnemann-Held, Peter J Collings, and Heinz-S Kitzerow. Self-organized assemblies of colloidal particles obtained from an aligned chromonic liquid crystal dispersion. *Soft Matter*, 11(8):1547–1553, 2015.

[98] Amanda J Tan, Eric Roberts, Spencer A Smith, Ulyses Alvarado Olvera, Jorge Arteaga, Sam Fortini, Kevin A Mitchell, and Linda S Hirst. Topological chaos in active nematics. *Nature Physics*, 15(10):1033–1039, 2019.

[99] Yu A Nastishin, H Liu, T Schneider, V Nazarenko, Rk Vasyuta, SV Shiyanovskii, and O D Lavrentovich. Optical characterization of the nematic lyotropic chromonic liquid crystals: Light absorption, birefringence, and scalar order parameter. *Physical Review E*, 72(4):041711, 2005.

[100] Daniel B Allan, Thomas Caswell, Nathan C Keim, Casper M van der Wel, and Ruben W Verweij. soft-matter/trackpy: v0. 6.1. *Zenodo, Feb*, 2023.

[101] Angel Martinez, Peter J Collings, and AG Yodh. Brownian dynamics of particles "dressed" by chiral director configurations in lyotropic chromonic liquid crystals. *Physical review letters*, 121(17):177801, 2018.

[102] Marco A Catipovic, Paul M Tyler, Josef G Trapani, and Ashley R Carter. Improving the quantification of brownian motion. *American Journal of Physics*, 81(7):485–491, 2013.

[103] Taras Turiv, Israel Lazo, Alexander Brodin, Bohdan I Lev, Volker Reiffenrath, Vassili G Nazarenko, and Oleg D Lavrentovich. Effect of collective molecular reorientations on brownian motion of colloids in nematic liquid crystal. *Science*, 342(6164):1351–1354, 2013.

[104] Hend Baza, Taras Turiv, Bing-Xiang Li, Ruipeng Li, Benjamin M Yavitt, Masafumi Fukuto, and Oleg D Lavrentovich. Shear-induced polydomain structures of nematic lyotropic chromonic liquid crystal disodium cromoglycate. *Soft Matter*, 16(37):8565–8576, 2020.

[105] John L Anderson. Colloid transport by interfacial forces. *Annual review of fluid mechanics*, 21(1):61–99, 1989.

[106] Yahaya Ibrahim, Ramin Golestanian, and Tanniemola B Liverpool. Multiple phoretic mechanisms in the self-propulsion of a pt-insulator janus swimmer. *Journal of Fluid Mechanics*, 828:318–352, 2017.

[107] Ramin Golestanian, TB Liverpool, and A Ajdari. Designing phoretic micro- and nano-swimmers. *New Journal of Physics*, 9(5):126, 2007.

[108] Thomas Bickel, Guillermo Zecua, and Alois Würger. Polarization of active janus particles. *Physical Review E*, 89(5):050303, 2014.

[109] Xiaolu Wang, Martin In, Christophe Blanc, Alois Wurger, Maurizio Nobili, and Antonio Stocco. Janus colloids actively rotating on the surface of water. *Langmuir*, 33(48):13766–13773, 2017.

[110] J. S. Lintuvuori, A. Würger, and K. Stratford. Hydrodynamics defines the stable swimming direction of spherical squirmers in a nematic liquid crystal. *Phys. Rev. Lett.*, 119:068001, Aug 2017.

[111] Ramin Golestanian. Anomalous diffusion of symmetric and asymmetric active colloids. *Physical review letters*, 102(18):188305, 2009.

[112] Oleg P Pishnyak, S Tang, JR Kelly, Sergij V Shiyanovskii, and Oleg D Lavrentovich. Electrically induced dynamics of colloidal particles dispersed in nematic liquid crystal. *Ukr. J. Phys.*, 54:101–108, 2009.

[113] I. I. Smalyukh, O. D. Lavrentovich, A. N. Kuzmin, A. V. Kachynski, and P. N. Prasad. Elasticity-mediated self-organization and colloidal interactions of solid spheres with tangential anchoring in a nematic liquid crystal. *Phys. Rev. Lett.*, 95:157801, Oct 2005.

[114] R. W. Ruhwandl and E. M. Terentjev. Long-range forces and aggregation of colloid particles in a nematic liquid crystal. *Phys. Rev. E*, 55:2958–2961, Mar 1997.

[115] V. A. Raghunathan Sriram Ramaswamy, Rajaram Nityananda and Jacques Prost. Power-law forces between particles in a nematic. *Molecular Crystals and Liquid Crystals Science and Technology. Section A. Molecular Crystals and Liquid Crystals*, 288(1):175–180, 1996.

[116] Ewan J Hemingway, Prashant Mishra, M Cristina Marchetti, and Suzanne M Fielding. Correlation lengths in hydrodynamic models of active nematics. *Soft Matter*, 12(38):7943–7952, 2016.

[117] Chaitanya Joshi, Daniel Goldstein, Cole Wennerholm, Eoghan Downey, Emmett Hamilton, Samuel Hocking, Anca Andrei, James H Adler, and Timothy J Atherton. Morpho–a programmable environment for shape optimization and shapeshifting problems. *arXiv preprint arXiv:2208.07859*, 2022.